MPHIL

Development of scalable graphene-based electronics for sensing applications

Stephenson, James

Award date:
2017

Awarding institution:
University of Bath

Development of Scalable Graphene-based Electronics for Sensing Applications.

James Frederick John Stephenson

A thesis submitted for the degree of Masters of Philosophy

University of Bath

March 2017

Supervisor: Dr A. Nogaret

Co-Supervisors: Dr A. Johnson and Prof S. Bending

Abstract

This MPhil focused on optimisation of graphene synthesis and device fabrication via Chemical Vapour Deposition. The primary aim of this work was to determine an optimal process for the fabrication of graphene tunnelling devices. Using analytical techniques to determine the quality of graphene samples after each step in the fabrication methodology under development, insights from these results could be used to develop a procedure which affords graphene devices with improved sheet resistivity, defect density, surface roughness, monolayer coverage and continuity. The optimised method which is proposed in this MPhil is aimed specifically for use in the synthesis of graphene electrodes for tunnelling heterostructure fabrication.

High resolution Raman mapping of graphene grown Copper seed substrates showed drastic variation in graphene quality across areas corresponding to different Copper miller surface terminations. Further Raman, Atomic Force Microscopy (AFM) and electrical measurements were performed to investigate graphene quality degradation upon wet-transfer of graphene onto Silicon substrates, which showed that the formation of graphene wrinkles during wet transfer is primarily responsible for the degradation of graphene quality during this step. AFM studies were also performed to determine an optimal annealing process to remove Polymer residues from graphene post-transfer. The sheet resistivity of graphene devices fabricated via the proposed methodology is up to ~3 fold lower than that of commercially available graphene, furthermore graphene wrinkle formation may be avoided improving sample continuity and decreasing surface roughness.

Acknowledgements

Firstly, I would like to thank Dr Alain Nogaret for his support and supervision. His continuous encouragement has been extremely helpful. I would also like to thank my secondary supervisor Dr Andy Johnson and his research group in Chemistry for being incredibly welcoming and helpful to the author, as well as Mr Andrew Rushworth, who has helped with the graphene synthesis, for his efforts and expertise. I believe this year has been a fruitful collaboration between the Physics and Chemistry Departments at the University of Bath; I am thankful for the Nogaret and Johnson group for their enthusiasm and knowledge which helped make this possible. From the Nanofabrication suite I must also thank Dr Stephen Wedge for his supervision. Finally, I would like to thank Prof. Simon Bending for the use of his Laboratory, the Centre for Doctorial Training and the EPSRC for funding.

Contents

List of Abbreviations

AFM - Atomic Force Microscopy

CVD – Chemical Vapour Deposition

GNC – Graphitic Nanoparticle Composites

ITO – Indium Tin-Oxide

Gr – Graphene

Di – Dielectric

DI – Deionised

EM - Electromagnetic

NDR – Negative Differential Resistance

PDMS – Polydimethylsiloxane

PMMA – Poly(Methyl methacrylate)

Overview

The remarkably high conductance, flexibility, strength and optical transmittance of graphene has drawn huge attention from the scientific community since the first successful isolation in 2004. In particular, graphene and other 2-D materials show promise for the development of pressure sensitive electronics. Graphene tunnelling heterostructures demonstrate robust negative differential resistance with a highly sensitive relationship to strain. In this MPhil, work is carried out to investigate the fabrication of graphene-based pressure sensitive electronic devices. This work focussed on the synthesis, lithographic processing and characterisation studies on CVD graphene with the purpose of determining a methodology for tunnelling heterostructure fabrication.

Raman spectroscopy and Atomic Force Microscopy (AFM) measurements were used to characterise and compare commercially available CVD graphene with graphene grown in collaboration between myself and Mr Andrew Rushworth of the Johnson Group at the University of Bath Chemistry Department, on high temperature (1050 ˚C) annealed Cu substrates[1]. High resolution Raman mapping of the G/2D Raman peak intensity ratio showed a high selectivity of graphene thickness between different Cu surface terminations with monolayer coverage of non-commercial graphene varying from 2.4% to 93.0% between different Cu grains. Furthermore defect density varied significantly across grain boundaries, between for surface terminations. This lead to conclusion that in order to produce large areas of graphene, homogeneous in quality and thickness[2], maximising grain size *via* high temperature annealing is an imperative step in CVD of graphene.

Prior to wet-transfer Raman peak ratio distributions showed commercial graphene was more homogeneous than the non-commercial graphene, with an average defect density of $< 6.45 \times 10^9\ cm^{-2}$ and monolayer coverage of 89.5%. Further Raman spectroscopy, AFM and electrical characterisation was performed after wet-transfer of commercially available graphene on Si/SiO_2 and fabrication of Hall bars, revealing a ~2-4 fold increase in average defect density

[1] For simplicity graphene grown by myself and Andrew Rushworth is referred to as non-commercial graphene for this point onwards.
[2] To clarify whilst the material of graphene is typically considered to be a single graphite layer; two or more sheets of graphite stacked onto one another are also considered to be "graphene" with different properties than "monolayer" graphene.

and a ~ 2 fold increase average thickness (from monolayer to bilayer). High resolution Raman mapping demonstrated that wrinkle formation was the primary cause of the degradation of the graphene post transfer as Raman mapping showed a high contrast in defect density between non-wrinkled and wrinkled areas of graphene. AFM and electrical measurements also showed high variation in the local properties of commercial graphene (surface roughness values between 1.7 to 3.15 nm of untreated graphene post Hall-bar fabrication and sheet resistivity values between 167.7 Ω sq^{-2} to 16.87 kΩ sq^{-2}). These results prompt the necessity to either select non-wrinkled regions of graphene for heterostructure fabrication or to minimise wrinkle formation during wet-transfer. Unfortunately wrinkle formation in graphene is the result of a high surface roughness of the Cu substrate being used in commercial CVD synthesis of graphene, and unless a high temperature annealing step is introduced to reduce the surface roughness of Cu substrate prior to graphene growth, wrinkle formation is unavoidable. To include this step, graphene must be grown *via* an improved CVD methodology similar to that used in this MPhil as opposed to methodologies used to fabricate graphene commercially; possible improvements are discussed.

PMMA residues were found on graphene after wet transfer, which could provide an obstacle when it comes to controlling the barrier height in tunnelling heterostructures. Therefore, AFM characterisation was also performed to determine the effectiveness of high temperature annealing and wet chemical treatment in the removal of residues from the surface of graphene in order to increase the homogeneity of a tunnelling barrier thickness. Whilst the effectiveness of treatment in chloroform remains non-conclusive, annealing graphene at 300 ˚C for 5 hours was shown to remove all residues, reducing surface roughness on non-wrinkled areas of graphene from ~ 2 nm to as low as 0.2 nm.

This work was necessary as preparation for tunnelling heterostructure fabrication, using the results from this work step-by-step routes are proposed towards the fabrication of tunnelling graphene-dielectric-graphene heterostructures using Chemical Vapour Deposition (CVD) of dichalcogenide dielectrics and spin coated polymer dielectrics.

1 Introduction

Soon after the first transistor was fabricated in 1947 by John Bardeen, William Brattain and William Schockley, electronics became increasingly integrated into society and everyday life [1]. As a result the electronics industry is now a multi-billion dollar industry and ever growing. As the electronics industry has grown and developed, demand has risen for a myriad of new applications. In particular, the miniaturisation of electronics, which was correctly predicted to grow exponentially by Gordon Moore in 1965, has stimulated the growth of the market for electronics [3]. There is now a demand for flexible, pressure-sensitive electronics for a number of useful applications such as touch-sensitive skin grafts, flexible personal electronic devices, and aeroplane wing air-drag reduction to name a few [4] [5] [6].

Graphene, a 2-D allotrope of carbon, consisting of single sheets of sp_2 hybridised carbon atoms in a hexagonal honeycomb structure, shows potential as a flexible semiconductor which could be used for pressure sensitive electronic devices. Owing to the unique behaviour of electrons in monolayer graphene, graphene is highly conductive, as well as flexible, strong and transparent. Whilst Indium-Tin Oxide (ITO) is currently being used as a flexible transparent conductor, graphene is a stronger and more flexible material [7]. Additionally, whilst ITO is comprised of rare and expensive elements, graphene synthesis can make use of renewable carbon feedstocks *e.g.* glucose [8]. Therefore graphene could potentially be a more sustainable alternative to ITO for utilisation in the aforementioned pressure-sensing applications.

The work carried out in this MPhil was aimed to produce results which could then be used to propose methodologies for graphene-dielectric-graphene heterostructure (Gr-Di-Gr) fabrication where an ambipolar current changes with a deformation in the dielectric domain size. A previous study [9] showed that Gr-hBN-Gr tunnelling capacitors exhibit strain-dependant negative differential resistance (NDR); it is expected that this phenomena will be investigated in future studies after heterostructures have been fabricated and characterised. An important aspect of this MPhil is to ensure that the work carried out in this report may be used later for graphene synthesis and heterostructure fabrication using solely industrially scalable methods which have the potential to be applied in commercial settings. Therefore controlled methods of graphene and dielectric fabrication are discussed such as chemical vapour deposition (CVD) and spin-coating, rather than micromechanical exfoliation, as used by [9].

This MPhil focusses on the characterisation of CVD graphene to ensure the quality available is appropriate for heterostructure fabrication. Electrical characterisation was carried out through Hall bar fabrication and subsequent testing. This work also served to develop and optimise methods which may be employed in heterostructure fabrication (i.e. optical lithography of graphene into desired patterns graphene). Since the desired dielectric thickness should ideally be less than 10 nm for a significant tunnelling current, AFM characterisation of CVD graphene surface topography was employed. AFM measurements provided feedback on the effectiveness of post lithography residue removal methods. Raman measurements were used to determine the thickness and defect density of CVD graphene; Raman maps provide detailed information about the homogeneity and distribution of these properties i.e. monolayer coverage, variation in defect density etc. Electrical measurements were also performed. Whilst the in-plane transport properties of graphene tunnelling heterostructures would not have a significant impact upon tunnelling current, sheet resistivity similar to typical quoted values of commercially available graphene (460 $\Omega/sq^2 \pm 40$ over 1 cm^2 areas) was considered optimal in this study.

To summarise, the specific aims of this MPhil were:

- Develop and optimise a detailed methodology which reliably affords CVD graphene of desired architectures, for electrical characterisation i.e. Hall bars and field-effect devices.
- Use Raman and AFM measurements to characterise commercially available CVD graphene and graphene synthesised in collaboration between myself and Mr Andrew Rushworth of the Johnson Group at the Department of Chemistry, University of Bath. This will help determine whether CVD graphene should be purchased or fabricated in further studies into heterostructure fabrication.
- Perform electronic characterisation on CVD graphene after Hall bar/field-effect device fabrication and compare the results with the quoted properties of commercially available graphene.

2 Background

It is easy to understand why it is appealing to use graphene in the development of pressure sensitive electronics: graphene has high conductance, tensile strength, and flexibility and it can be produced from renewable feedstocks. The theory necessary to understand the properties of graphene is discussed in the literature review. This project is concerned with the synthesis of graphene *via* CVD, an industrial scalable method, therefore CVD is discussed in section 2.4.1 and compared against other methods. The characterisation methods are also explained in section 2.5, specifically when applied to analysing graphene. Three important phenomena which will most likely be exploited in further work when performing electrical measurements on graphene and Gr-Di-Gr heterostructures are also discussed in this section: the Gate field-effect, Hall Effect and Negative Differential Resistive (NDR)

2.1 Discovery of Graphene

Graphene is an allotrope of carbon. Carbon allotropes can be grouped into families based on the number of dimensions they span (over a distance much larger than atomic scale). Three-dimensional allotropes include diamond, graphite and amorphous carbon. Graphene is a two-dimensional allotrope of carbon since single monolayer graphene crystals consist of a single atomic layer but cover areas up to ~50cm^2 [10].

In 1947 the band structure of a single layer of graphite was determined theoretically as an initial study, which was then built upon in order to find the band structure of bulk graphite [11]. However, the isolation of single graphite layers was considered unlikely as this would disobey the Mermin-Wagner theorem which states that any 2-D crystal is thermally unstable, at any small non-zero temperature [12]. However, in 2004, graphene monolayers were isolated by exfoliating a bulk graphite crystallite with sticky tape and then transferring the flakes of graphite/graphene from the sticky tape onto a silicon substrate [13].

After graphene was first isolated and its electrical properties were reported, a worldwide effort within the scientific community focussed on the fabrication, theoretical aspects and applications of graphene. Figure 2.1.1 shows how the number of papers published worldwide concerning graphene increased rapidly after the discovery in 2004.

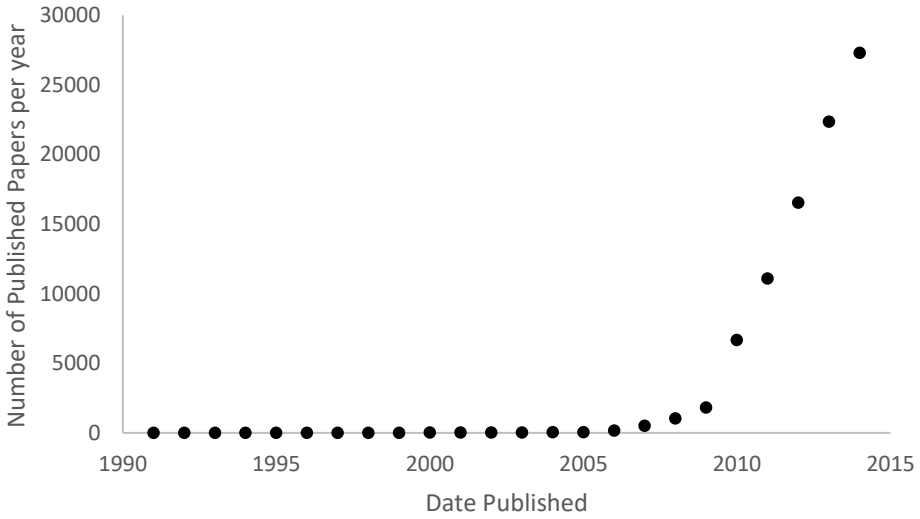

Figure 2.1.1: Number of papers published with the keyword "graphene" in the title over the last 25 years. [3]

2.2 **Properties of Graphene**

Electrical characterisation revealed the appealing properties of graphene (as discussed previously) and this sparked the rise in graphene-related research after 2004. Charge carrier mobilities up to ~200,000 cm V^{-1} s^{-1} [14] have been measured in suspended graphene and ~15,000 cm V^{-1} s^{-1} when mounted on a Silicon substrate [13]. Graphene shows a clear gate-field effect, such that electron and hole densities can be continuously tuned up to densities as high as 10^{13} cm^{-2} [13]. Additionally graphene is flexible, transparent and is the strongest known material with a Tensile strength and Young's modulus of 130GPa and 1TPa respectively [15]. In order to understand the properties of graphene it is important to discuss its structure in greater detail.

In real-space[4], graphene is comprised of a honeycomb structure of carbon atoms; this structure can be defined by two triangular sub-lattices, A and B. The graphene lattice is shown in Figure 2.2.1.

[3] Journal search was performed using Web Of Science.
[4] Graphene is discussed in real space and reciprocal space in this section.

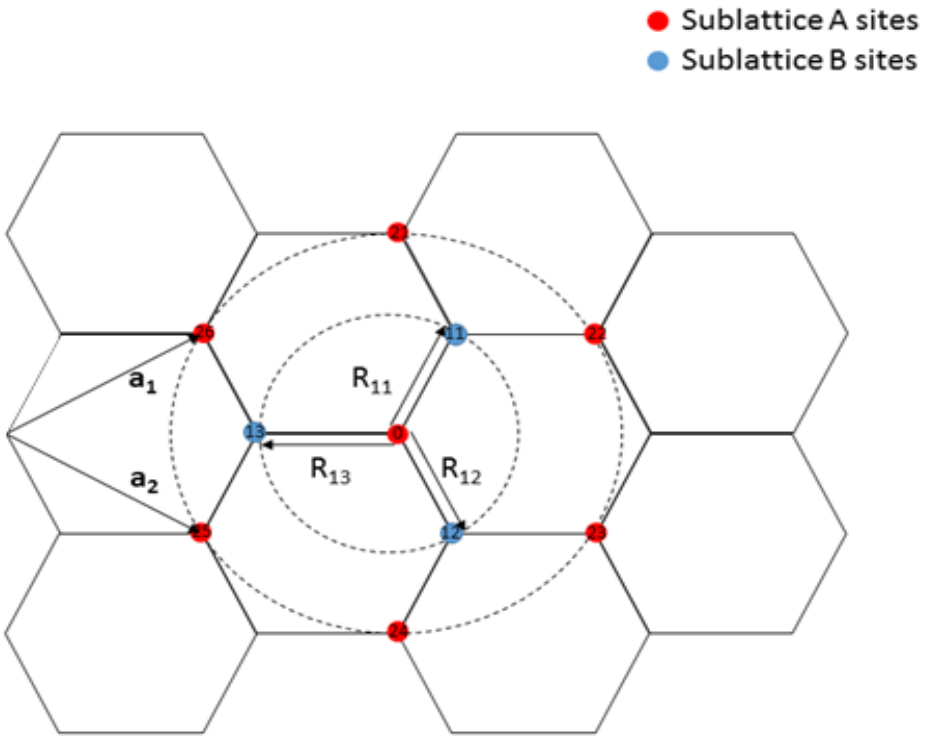

Figure 2.2.1: Graphene lattice and unit cell vectors in real space where $a_{1,2} = a_0\left(\frac{\sqrt{3}}{2}, \pm\frac{1}{2}\right)$, where $a_0 = 2.412$ Å is the unit lattice vector. Sublattices A and B are labelled and neighbouring atomic sites and inter-neighbour vectors R_{ij} are labelling using an index showing 1st and 2nd nearest neighbours *1j* and *2j* respectively to a central atomic site labelled 0.

Three of the four valence electrons in sp_2 hybridised carbon are fixed in sp_2 bonds (σ bonding orbitals); the fourth electron is in a π bonding orbital. Electrons in the π/π^* bonding/anti-bonding orbitals govern the electronic behaviour of graphene at room temperature. This is because at the corners of the Brillouin zone of graphene (K-points), whilst the σ bonding/anti-bonding orbitals are located at energies too far from the Fermi energy of graphene in an energy band diagram (3.5 eV), the π anti-/bonding orbitals correspond to the conduction and valence band with a zero bandgap [16]. The reciprocal lattice refers to the Fourier transform of the Bravais lattice of graphene and exists in momentum space (k-space). The unit-cell of the reciprocal lattice of graphene is named the Brillouin zone (BZ). A complete set of solutions of waves in a periodic medium can be characterised through their behaviour within a single BZ i.e. Bloch functions. The electronic properties of graphene are investigated through finding the energy dispersion (E-k) relations along lines crossing salient points (Γ-M-K) within the BZ. The reciprocal lattice and BZ of graphene is shown in Figure 2.2.2.

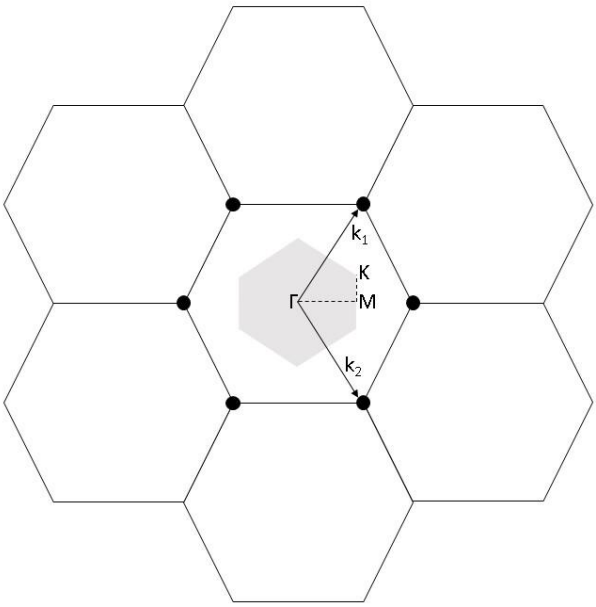

Figure 2.2.2: Graphene reciprocal lattice with reciprocal lattice vectors $k_{1,2} = \frac{2\pi}{a_0}\left(\frac{1}{\sqrt{3}}, \pm\frac{1}{2}\right)$. The shaded region refers to the BZ of graphene with the $\Gamma - \mathrm{M} - K$ axis labelled which is often used to describe the band structure of graphene. The co-ordinates of the high-symmetry points in the BZ zone are determined geometrically: $\mathrm{k}(\Gamma) = (0,0), \mathrm{k}(M) = \frac{2\pi}{a_0}(\frac{1}{\sqrt{3}}, 0), \mathrm{k}(K) = \frac{2\pi}{a_0}(\frac{1}{\sqrt{3}}, \frac{1}{2\sqrt{3}})$

The tight binding (TB) model is used to calculate the energy dispersion relations of the valence and conduction bands of graphene throughout the BZ. The TB model is typically applied to electrons within crystalline solids and individual molecules. Contrasting the nearly free electron model, the TB model assumes that electrons spend most of their lives bound to their ionic cores and interactions with atoms further than nearest neighbours diminish rapidly and may be omitted from calculations. The electron wavefunction Ψ is therefore approximated through the superposition of atomic orbitals[5]. The derivation of the E-k relation (Equation 2.2.1) through the TB model is given in the annex. It is

$$E(k_1, k_2)^{\pm} = \frac{\varepsilon_{2p} \pm \gamma_0 \sqrt{u_{12}(k_1, k_2)}}{1 \pm s_0 \sqrt{u_{12}(k_1, k_2)}}, \qquad \text{Equation 2.2.1}$$

where, the wavevector *k* is given in terms of reciprocal unit lattice vectors,

$$u_{12}(k_1, k_2) = 2cos(2\pi.k_1) + 2cos(2\pi.k_2) + 2cos\left(2\pi.(k_1 - k_2)\right) \qquad \text{Equation 2.2.2}$$

[5] Bloch Functions are suitable descriptions of a wavefunction of a particle in periodic potential.

$$\boldsymbol{k} = k_1.\boldsymbol{k_1} + k_2.\boldsymbol{k_2}$$ Equation 2.2.3

k_1 and k_2 are scalars of the reciprocal lattice unit vectors $\boldsymbol{k_1}$ and $\boldsymbol{k_2}$.

Using the Equation 2.2.1 the energy dispersion relation of graphene may be plotted throughout the Brillouin zone. The E-k relation determined through *ab intio* first principles studies and through the nearest-neighbour TB model is shown along the high symmetry direction in Figure 2.2.3.

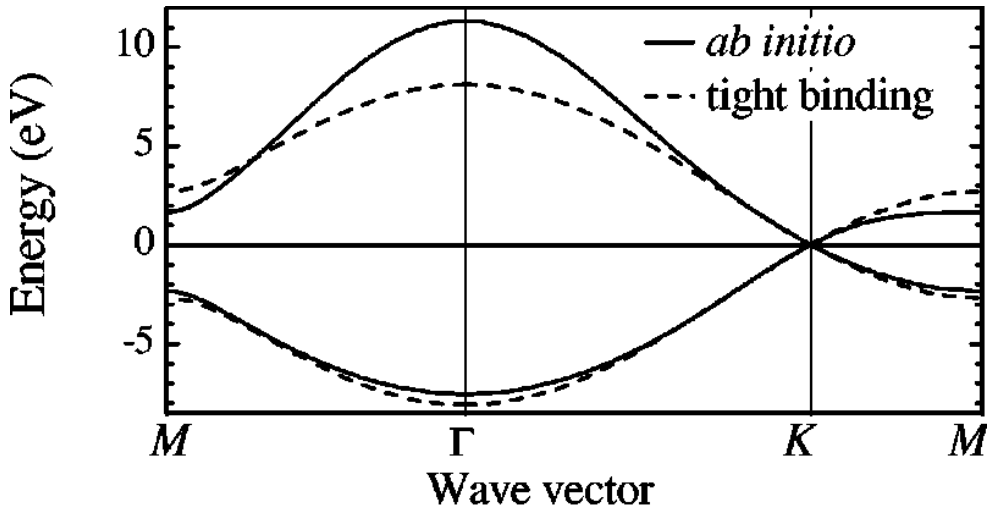

Figure 2.2.3: Energy dispersion relation of graphene determined through *ab initio* studies and the tight binding model with values $\varepsilon_{2p} = 0, s_0 = 0$ eV, $\gamma_0 = 2.7$ eV [17]

The energy of the conduction band (CB) and valence band (VB) is coincided at the K point[6] i.e. when $k_1 = \frac{1}{3}, k_2 = -\frac{1}{3}$.

$$u(K) = u\left(\frac{1}{3}, -\frac{1}{3}\right) = 2cos\left(\frac{2\pi}{3}\right) + 2cos\left(-\frac{2\pi}{3}\right) + 2cos\left(\frac{4\pi}{3}\right) + 3 = 0$$ Equation 2.2.4

Therefore,

$$E(K)^{\pm} = \varepsilon_{2p}$$

This reveals that the energy of the conduction and valence band are both equivalent to the Fermi energy at the K point, therefore graphene is a zero-bandgap semiconductor. This property has several important implications including restricting the ON-OFF ratio of monolayer graphene transistors. Furthermore, close to the K point the energy dispersion relation is approximately linear and may be expressed as $E = \pm\hbar v_F|k|$. This linear dispersion

[6] Determined through considering the geometry of the BZ.

relation is described by the relativistic Dirac equation, which reveals electrons in graphene have a zero effective mass and a group velocity of $V_G \approx \frac{1}{300} c$ (where c represents the speed of light) [18]. These properties are responsible for the high electron mobility found in graphene (in excess of 200,000 $cm^2\ V^{-1}\ s^{-1}$) [70].

2.3 **Electronic properties of Bi/Few-layer graphene**

Bilayer graphene and few-layer graphene (<10 layers) are distinguished electronically from both monolayer graphene and graphite. Near the K-points whilst monolayer graphene shows a linear energy-dispersion relation with a zero bandgap, bi-layer and few-layer graphene have a parabolic dispersion relation. The E-k relation of monolayer and bilayer graphene is shown in Figure 2.3.1 [72] [73].

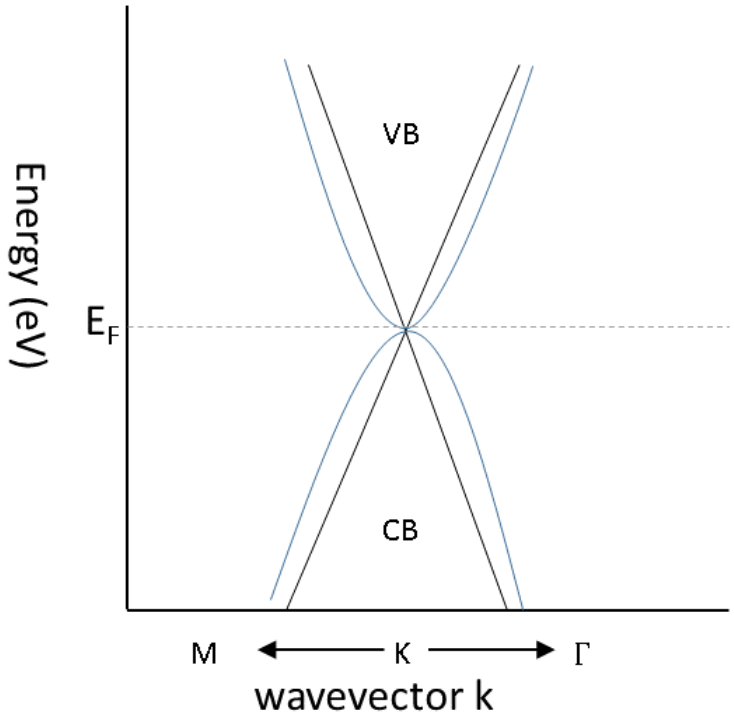

Figure 2.3.1: Energy dispersion relation of the VB and CB of monolayer (black) and bilayer (blue) graphene within close proximity of a K point in reciprocal space with the Fermi energy labelled.

Consequently, whilst electrons behave as massless Dirac Fermions in monolayer graphene, electrons in multi-layer graphene with a parabolic E-K relation have a finite effective mass which can be determined through the following expression:

$$m_{eff} = \left(\frac{\partial^2 E}{\partial p^2}\right)^{-1} \qquad \text{Equation 2.3.1}$$

where,

$p = \hbar k$, such that $m_{eff} = 0.054 m_e$ [20].

Un-doped bilayer graphene is a zero bandgap semiconductor,

. However by applying a perpendicular electric field, a bandgap is opened which may be tuned continuously by varying the gate voltage between 0 and 250 meV [21]. The ability to open a bandgap in graphene opens the possibility for transistors with high ON-OFF ratios.

As more layers are stacked upon one-another, the band structure changes and gradually tends towards the band structure of bulk graphite, a semimetal with a 3 meV overlap between the conduction and valence band [22].

To summarise:

- Tight-binding calculations show that electrons in graphene have a linear dispersion relation near the K points in the BZ with a zero-energy bandgap.
- The linear dispersive nature of electrons in graphene reveals that electrons in monolayer graphene behave as massless Dirac Fermions, which leads to several unique phenomena.
- The energy dispersion relation of multi-layer graphene near the corners of the BZ is parabolic, therefore the electrons in bilayer graphene behave with a finite mass.
- Bilayer graphene has a gate-tuneable bandgap.

2.4 **Synthesis of Graphene**

Graphene was first fabricated in 2004 by a method commonly known as the “scotch-tape” method. This method takes advantage of the structure of graphite which consists of stacked graphene planes held together by weak van-der-Waal forces. These planes slide over each other easily and therefore can be cleaved or exfoliated from bulk graphite with ease. The process is relatively simple; a piece of nitto tape is stuck onto a bulk graphite crystallite and then removed. Flakes of graphene/graphite are removed from the crystallite and remain on the tape. In order to reliably isolate monolayer graphene, a new piece of tape is stuck onto the original piece and then peeled off, leaving fewer, thinner flakes on the second piece. This process is repeated consecutively with several new pieces of tape and then the final piece of tape is placed onto a silicon substrate with an oxide layer. At this point the substrate is observed under an optical microscope and suitable flakes are found and fabricated into devices. To make this step feasible

the silicon substrate has an oxide layer approximately 300nm thick. Owing to the similarity of the thickness of the oxide layer and the wavelengths of visible light, the graphene interface causes an interference pattern in the SiO_2 layer. This interference introduces a relationship between the SiO_2 dielectric thickness and optical contrast between regions of SiO_2 with and without a graphene interface. This relationship may exploited by selecting an optimal dielectric thickness for mounting graphene flakes to improve the visibility of graphene through optical inspection. Optical characterisation of graphene is explained in greater detail in section 2.5.1. Substrate preparation prior to transfer often involves fabricating registration marks to make it easier to locate flakes at later stages, *e.g. via* Electron Beam Lithography. Micromechanical exfoliation can readily produce pristine graphene crystals which are used for proof-of-concept studies; however, the method shows little promise for mass production. This is due to the inherent lack of control over the size, shape and thickness of the flakes produced by this method.

After the discovery of graphene, many new synthesis methods have been discovered in the search for one which shows potential industrial scalability. The most promising methods involve controlled growth of graphene on a surface since this allows large areas of graphene to be produced in batches. Graphene can be grown on a surface by either altering the structure of carbon which already exists within the substrate *via* epitaxial growth or depositing carbon onto a substrate *via* chemical vapour deposition.

Epitaxial growth involves heating a SiC crystal to temperatures between ~ 1273-1773K under ultra-high vacuum, causing Si on the crystal surface to sublimate [23]. A carbon-rich surface is left behind which self-assembles into multi-domain graphene *via* nucleation processes. To aid graphene growth on the surface, Ni is evaporated onto the SiC (a layer typically a few hundred nanometres thick) surface prior to heating, since the Ni(111) surface lattice is very similar to graphene [24]. The geometric similarity between Ni(111) and graphene promotes the self-assembly of graphene structures grown as carbon diffuses through the Ni surface, forming layers using the Ni(111) surface as a structural basis. Unfortunately, transferring graphene from the SiC wafer onto another substrate is difficult. It is possible to transfer graphene produced *via* epitaxial growth onto other substrates, however this process is expensive and requires the use of rare metals as it is accomplished by depositing a Cr/Au layer on top of the graphene surface and then peeling the graphene layers off along with the metallic film [25]. The limited choice of substrate makes it difficult to integrate graphene grown *via* epitaxy into silicon based electronics and prevents utilisation of the flexibility of graphene.

However, CVD can be used to fabricate large areas of high-quality graphene in a controlled manner on a variety of substrates and shows potential to be implemented for sustainable industrial scale production.

2.4.1 Chemical Vapour Deposition

Materials are grown using CVD by exposing a catalytic substrate to gaseous chemicals. Decomposition reactions occur either in the gaseous phase (homogenous CVD) or on/in the vicinity of the substrate surface (heterogeneous CVD), which leads to the deposition of a product on the surface. Energy is provided for decomposition reactions in different forms including heat and light in thermal assisted CVD and electrical discharge in plasma assisted CVD. After deposition, atomic species migrate over a substrate surface. This leads to the nucleation of crystals which grow and join together until a continuous polycrystalline layer has formed. Nucleation sites typically originate from defects in the substrate, *i.e.* grain boundaries.

In the first successful attempts to synthesise graphene *via* CVD in 2008-2009, carbon from hydrocarbon precursors, most commonly CH_4, was deposited onto Ni substrates at high temperatures [27] [28]. Soon after, CVD graphene was synthesised on a variety of transition metal substrates *i.e.* Cu, Co, Pt, Ru(0001) *etc* [16] [29] [30] [31]. However, considering the trade-off between graphene quality and substrate cost, Ni and Cu were quickly considered as the most promising growth substrates.

Differences between the CVD growth mechanisms in Ni and Cu can be accounted for by a high and a low carbon solubility, respectively [32]. After precursor decomposition, carbon dissolves through the surface of Ni at high temperatures. Then, as Ni is cooled, carbon precipitates out onto the Ni surface since carbon solubility decreases with temperature and self-assembles on the Ni surface to form graphene [26]. Whilst the primary graphene growth mechanism on Ni is a segregation process, catalytic surface decomposition of hydrocarbons accounts for graphene formation on Cu. Catalytic activity drops dramatically after monolayer coverage on Cu causing CVD growth to be self-limiting by nature. Multi-layer growth suppression is more difficult on Ni since the growth mechanism is only limited by the carbon solubility of nickel. Therefore it is easier to grow monolayer graphene on Cu, and is hence the preferred growth substrate in modern graphene CVD reactions.

Whilst different groups and companies use a number of CVD methods, the method developed by the Johnson group employs the following steps, based on literature research, to maximise

quality and monolayer coverage of graphene grown *via* thermal assisted CVD. The full details of the optimised CVD process is provided in section 3.1.1.

- **Cleaning step –** Cleaning the Cu foil prior to deposition drastically improves graphene quality [33]. Cyclic washing using acetone, isopropanol and deionised (DI) water and drying with N_2 removes any organic residues effectively. Acids and bases were shown to be most effective at removing impurity particles/ions. These impurities act as nucleation sites for bilayer graphene growth, and therefore removal increases monolayer graphene coverage [33]. Defect sites also cause discontinuities to form in CVD graphene and surface doping, reducing charge carrier motilities [33]. Washing the metal substrate with Ni etchant solution or dilute nitric acid, cyclic solvent/DI water and drying in N_2 is therefore a necessary cleaning step prior to graphene growth [33]. Etching the Cu surface briefly also removes milling features, reducing the surface roughness of the substrate[7].

- **Heating step -** After cleaning, Cu is heated to a high temperature for annealing in a closed hot-wall vessel (typically a quartz cylinder inside a furnace). In order to ensure contaminant reactions do not occur during heating, atmospheric gasses inside the reaction chamber are first evacuated through vacuum pumping. An inert gas or gas mixture is then flowed through whilst the temperature is increasing and continuous pumping is maintained.

- **Annealing step –** To ensure the foil surface is clean and catalytically active (devoid of any oxide layers) high temperatures in the presence of H_2 are maintained for durations typically at least over an hour. The high temperatures helps rearrange Cu surface morphology, increasing grain size and removing structural defects [34]. H_2 in the annealing process causes Cu grains to grow, reaching a few mm^2 [62]. Certain Miller index terminations of Cu, especially low index surfaces such as (111) promote the growth of large or even single graphene domains [63] [64], therefore increasing Cu grain size can help increase average graphene domain size, reduce the number of grain boundaries and consequently reduce the defect density. Additionally annealing in H_2 at

[7] Surface roughness of Cu substrates is known to cause wrinkle formation during transfer onto a substrate, therefore steps should be taken to flatten the topography of the substrate prior to CVD.

high temperatures reduces surface roughness, which decreases wrinkle formation in the growing step and transfer step [35].

- **Growing step –** A hydrocarbon precursor, usually methane is introduced after annealing; hydrogen flow is maintained throughout this step. Homogenous methane decomposition occurs at very high temperatures (>1200 ˚C), however in the presence of a metallic catalyst such as copper, methane decomposes at much lower temperatures (< 900˚C). This is fortunate because at very high temperatures (>1050 ˚C) copper sublimates more readily [27], causing the substrate to increase in surface roughness. However, similarly high temperatures also promote lower graphene nucleation site density, therefore growth temperature is optimised based on a compromise between these two factors [27]. Precursor pressures, temperature, residence time and air flow are all parameters which must be optimised to achieve successful deposition of high quality graphene films with the desired thickness. Whilst Cu catalytic activity decreases as monolayer graphene is grown, multi-layer graphene growth is not entirely supressed and multi-layer domains nucleate and form thicker films after prolonged exposure to carbon species. Therefore, residence time must be long enough for continuous growth of graphene films, whilst limiting the methane-surface exposure to ensure the correct number of atomic layers are deposited. At the University of Bath, Andrew Rushworth in the Johnson group constructed the CVD set up shown in Figure 2.4.1 and optimised growth parameters to grow continuous monolayer graphene on annealed Cu substrates.

- **Cooling step** - After an optimised residence time, methane flow is turned off, but H_2 is continuously pumped through the vessel as it cools down as an inert species. The temperature should be allowed to reduce to less than 200 ˚C before the chamber can be backfilled with atmospheric air to ensure oxidation does not occur.

After cooling, graphene may be transferred from the metal seed substrate onto another substrate, most frequently Si/SiO_2. A number of transfer techniques have been developed, however the simplest and most successful is a wet transfer method. This technique involves spin-coating poly-methylmethacrylate (PMMA) onto the metal substrate after CVD growth. Once the PMMA has dried, the Cu-Gr-PMMA stack is baked in an oven to improve adhesion between PMMA and graphene. The graphene on the underside of the substrate is then etched using nitric acid, then immediately quenched in de-ionised water. The copper substrate is then etched in ammonium persulfate, leaving a PMMA-Gr film floating in solution. Cyclic washing

with DI water and dilute HCl is necessary to remove residual ions since containment ions detrimentally affect graphene due to hole doping and the introduction of defects [36]. Ferric chloride and ferric nitride may be used as etchant solvents, however ammonium persulfate is typically preferred since ammonium residues are easier to remove than iron residues [36]. The film is then transferred onto a substrate of choice, left to dry and then baked for improved adhesion between graphene and the substrate. Washing in acetone removes most of the PMMA, while heating in acetone under reflux removes PMMA more effectively. However, AFM studies have shown that due to strong chemisorption interactions between PMMA and graphene, even after heating in solvents, PMMA residues up to ~4 nm remain on the graphene. Hole doping from PMMA causes degradation of electrical properties of graphene [37] and therefore studies have investigated the removal of PMMA residues through wet chemical treatment and high temperature annealing. AFM and gate field-effect measurements[8] show that annealing at 650 ˚C under constant Ar/H_2 flow removes almost all remaining residues, resulting in a ~30% reduction in sheet resistance [37]. However, studies have revealed that annealing at high temperatures causes stronger adhesion between graphene and the underlying substrate which degrade the charge carrier mobility due to p-doping between Si/SiO_2 and graphene [38]. Additionally comparisons between the D/G Raman peak intensity ratio of graphene before and after annealing suggests that high temperature annealing may introduce defects to graphene; this is likely due to oxidation of graphene which will occur if the system being used is not under ultra-high vacuum during annealing [37]. A compromise between removal of residue polymer and minimising substrate-graphene interactions may be reached by using lower annealing temperatures. A collaborative effort between myself and Andrew Rushworth of the Johnson group worked toward the optimisation of the CVD and the transfer process[9] for use in further work which involves CVD graphene synthesis. The full step-by-step synthesis and transfer procedure is described in section 3.1.

[8] Whilst not performed in [37], gate field-effect measurements would show the charge neutrality point in a Vg vs σ plot is reduced from a positive gate voltage to ~0V as p-doping is reduced with PMMA removal.
[9] The majority of the credit of this task is owed to Andrew Rushworth. I was however heavily involved in discussions and characterisation studies with a view to improve the process.

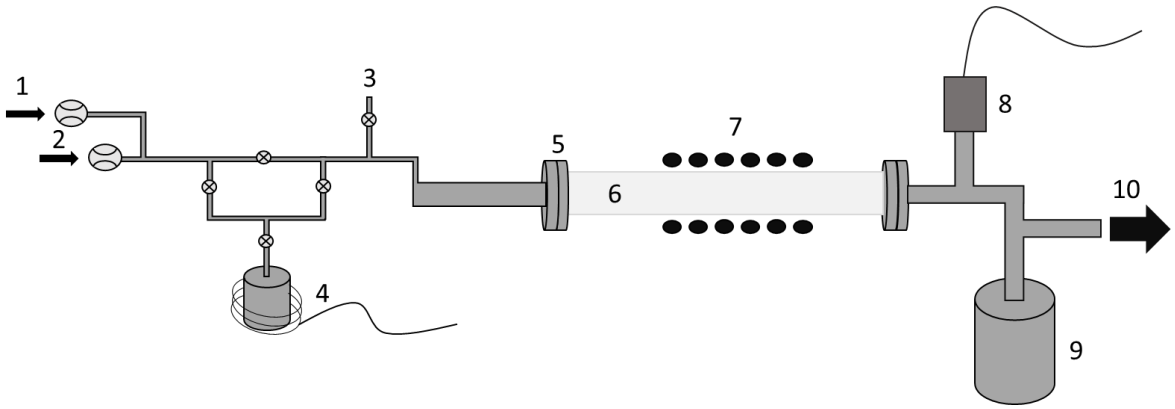

Figure 2.4.1: Thermal assisted CVD rig. Labels 1-10 represent: 1, 2 – Gas inlet controls. 3 – Valve to atmosphere. 4 –Solid/Liquid precursor pot. 5 – Rubber seals. 6 - Quartz reaction vessel. 7 -Heating elements in a finance. 8 – Temperature control. 9 – Liquid nitrogen trap. 10 – Pump. CVD of graphene does not make use of features 4 and 9.

2.5 **Characterisation of Graphene**

The properties and quality of graphene produced *via* CVD vary from process to process and often batch to batch, therefore it was important to characterise the graphene produced at the University of Bath and commercially available graphene in order to determine how graphene with optimal properties will be sourced for heterostructure fabrication. Characterisation of graphene typically involves finding the thickness and defect density *via* Raman studies, sheet resistivity and charge carrier concentration and mobility through fabrication of Hall bar devices, electrical testing and topological measurements *via* AFM. The use of these methods to characterise graphene is discussed in this section.

2.5.1 Optical Measurements

Being able to observe graphene optically makes further synthesis steps significantly easier. The opacity of graphene stacks thinner than five layers is too low for direct observation with the naked eye. By transferring graphene onto a silicon substrate with a thermal oxide layer with a thickness of approximately 300 nm the contrast of graphene samples as thin as monolayer may be increased such that observation with the naked eye is possible. The oxide layer acts as a dielectric, adding a third interface into a layered system as shown in Figure 2.5.1. Solving Fresnel's equations [39] for this system reveals that reflectance is a function of two interfering phase shifts ϕ_1 and ϕ_2 which changes with wavelength and optical path length, which is governed by the dielectric thickness. Therefore, the addition of a dielectric layer enables the maximisation of optical contrast through selecting an optimum oxide thickness. Figure 2.5.2 shows how optical contrast changes with oxide thickness and wavelength.

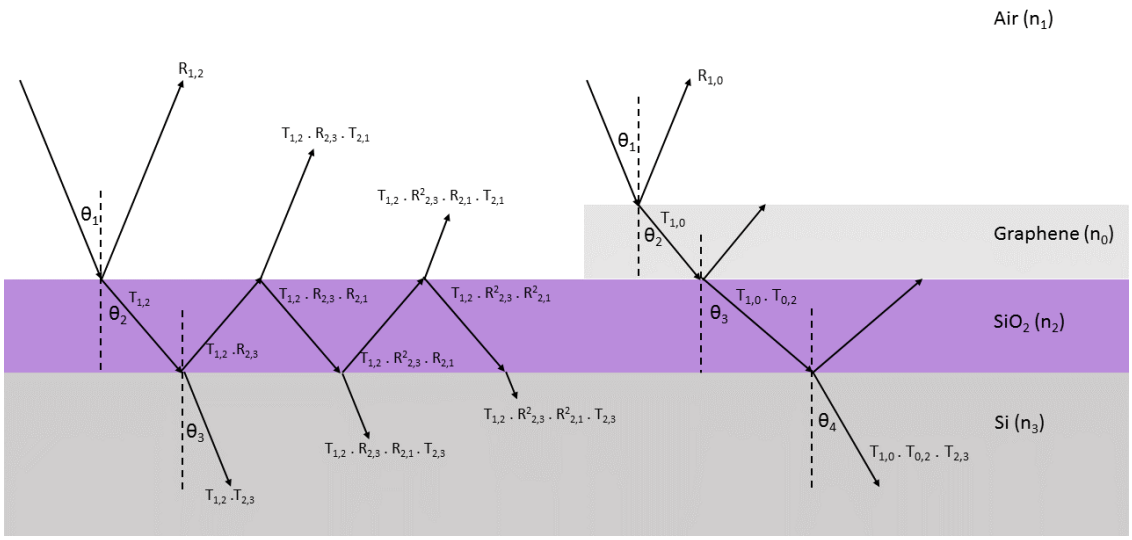

Figure 2.5.1: Diagram showing the transmittance/reflection at each interface for graphene on a Silicon substrate.

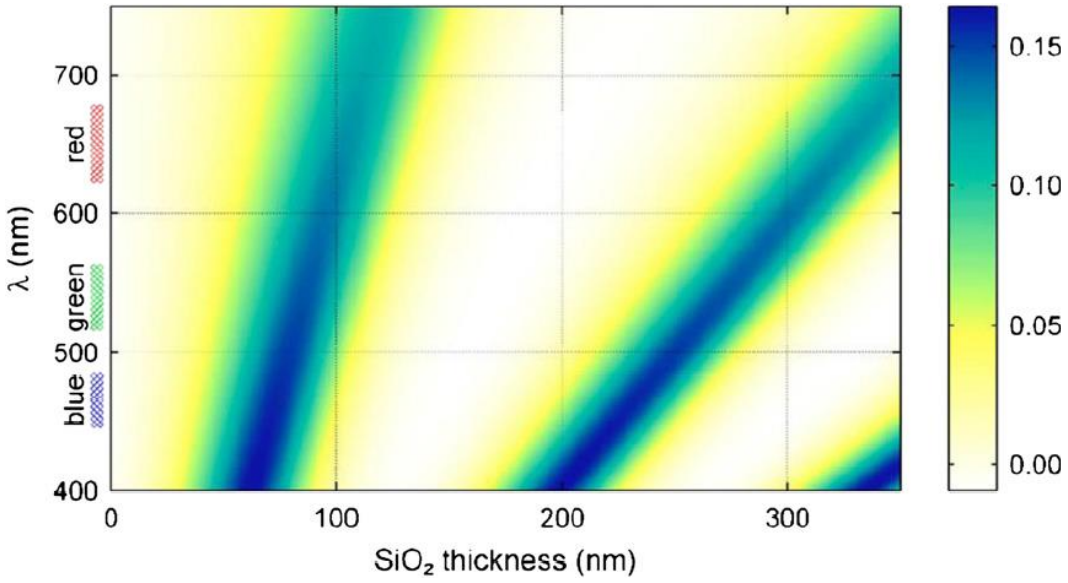

Figure 2.5.2: Colour plot of optical contrast of graphene on a Si/SiO_2 substrate as a function of dielectric thickness and wavelength of illuminating light [39].

Based on the results shown in Figure 2.5.2 graphene is transferred onto silicon substrates with a 300nm oxide thickness which, upon illumination with green light, causes an optical contrast of 12% which is enough for observation with the naked eye[10]. The increased contrast is essential for flake searching when using micromechanical exfoliation for instance, or in lithographic processing steps when fabricating graphene devices. Since thicker graphene samples have a higher optical contrast, it is possible to differentiate between domains of

[10] The contrast of graphene on Silicon with a 300nm oxide layer is sufficient for observation with the naked eye under white light.

graphene with different thicknesses when graphene is mounted on a Si/SiO_2 substrate, i.e. multi-layer islands and wrinkles over CVD graphene. However, to accurately determine the exact number of layers, other methods, i.e. Atomic Force Microscopy and Raman Spectroscopy are more suitable. Optical measurements however make further processing steps significantly easier.

Graphene produced by CVD is polycrystalline, crystal grain size is an important feature as crystal grain boundaries promote defect growth and attenuate in-plane electron transport. The simplest method to determine crystal grain size is to find the nucleation density. This is achieved by performing CVD runs on Cu substrates with low residence times or precursor pressures, so monolayer graphene islands nucleate but have not yet grown and joined to form a continuous sheet. In order to increase the optical contrast between graphene regions and bare Cu substrate, annealing in air is performed which exclusively oxidises regions of the Cu substrate which are not covered by graphene. The optical contrast between copper and copper oxides is sufficient to see graphene domains after this annealing step and hence approximate crystal domain size through the inter-island distance [40]. Whilst this procedure was not carried out in this work, it remains an option in future work to provide feedback for substrate preparation optimisation studies.

2.6 **Atomic Force Microscopy**

Atomic force microscopy is a tool which is used for nanoscale surface topography profiling. AFM is used in this project to characterise the surface of copper substrates and CVD graphene post transfer and processing.

Surface topography is mapped using AFM by measuring the force exerted on an atomically sharp tip from the surface. Van der Waals forces dominate short range interactions (tip-surface distance < 0.5nm) other long range forces such as electrostatic become more significant at larger separations. Extremely high sensitivity is required for nanometre-scale contrast i.e. step heights of ~0.8 nm [61] between regions of bare substrate and graphene, this is achieved through mounting the tip on a cantilever and measuring deflection through reflecting a laser off the cantilever onto a photodiode. AFM has three primary operating modes in order to determine surface topography which are described below and the operating distance of each mode is shown in Figure 2.6.1.

Contact mode: By allowing the tip to approach the surface using piezoelectric controls to a separation of <0.5 nm, repulsive van der Waals interactions cause the tip to be deflected. Feedback loops are used to maintain a constant deflection by adjusting the cantilever z-position and therefore determine the surface topography. Whilst this mode is effective for fast scan rates and is suitable from surfaces with a large surface roughness, contact between the tip and surface can cause sample degradation.

Non-contact mode: An AC voltage is supplied causing piezoelectric oscillations of the cantilever slightly above its resonant frequency. The cantilever oscillates between 1 and 10 nm above the surface with an amplitude of a few nm. Van der Waals and other longer range interaction reduce the resonant frequency of the cantilever and using feedback loops the resonant frequency is maintained by adjusting the cantilever z-position and therefore imaging the surface topography. This mode does not cause sample degradation.

Tapping mode: The cantilever is driven piezo-electrically at its resonant frequency at smaller tip-surface distances (0.5-2 nm). Similarly, to the other modes, feedback loops are used to maintain constant oscillatory amplitude to map surface topography. This mode is suitable for providing high resolution images of surfaces which are robust.

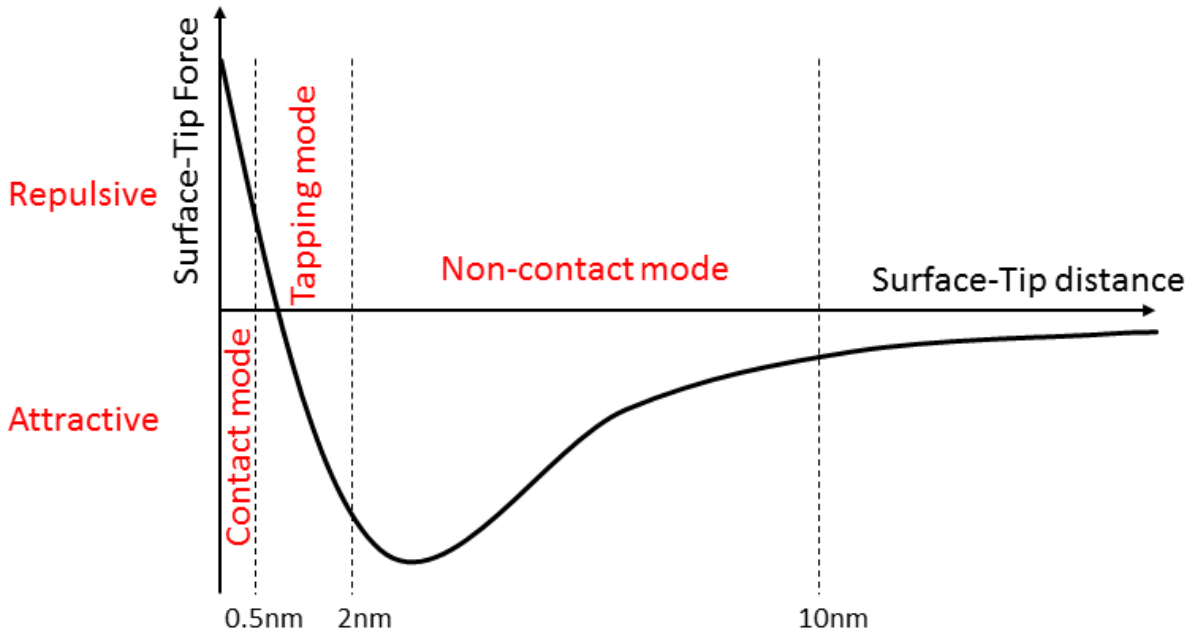

Figure 2.6.1: Typical plot of van der Waals force against distance, and the ranges in which each mode operates.

Different modes are selected based on the sample being mapped. For example, imaging the topography of a large area of a Cu substrate after annealing requires a fast mode which provides high quality images. Since sample degradation is not an issue in this case, tapping mode would be selected. However, when performing an AFM scan on a graphene Hall bar, non-contact mode would be used since changing the quality or properties of graphene prior to electrical characterisation must be avoided.

2.7 **Raman Spectroscopy**

Raman is a principle tool in the characterisation of graphene as it can accurately determine thickness, geometry and defect density non-invasively. By examining the Raman peak ratios of a spectra the thickness and defect density of graphene can be determined. Furthermore, by taking a series of Raman measurements over an area of graphene it is possible to spatially map defect density and thickness over a sample to determine the distribution of these properties over an area of graphene.

To interpret Raman spectra, it is important to first understand the underlying physics behind Raman spectroscopy, and specific Raman processes responsible for each peak in a spectra. Illumination of a target with a monochromatic laser causes phonon-mediated electron excitation to a virtual energetic state[11]. In the case of Rayleigh scattering, electrons are excited to a higher energetic state for a short time frame before falling back to the ground rovibrational state, causing a photon with the same energy as the incident absorbed photon to be scattered. Infrequently the energy between the incident and scattered photon are inequivalent (~ 1 in 10 million) [41]. The decrease/increase in photon energy can be accounted for by Stokes/anti-Stokes radiation where a quanta of energy is transferred from/to the incident photons *via* vibrational modes (phonons). In Stokes radiation, the rovibrational energetic state of the target crystal increases to a higher energetic state, and therefore the scattered photon wavelength is shifted down. The rovibrational energetic state of the target atomic system (typically molecules or crystals) decreases to a lower energetic state in anti-Stokes radiations, so it follows that the scattered photon wavelength is shifted up. At room temperature, most systems are in a ground rovibrational state $(v = 0)$ and therefore Stokes radiation to the first rovibrational state

[11] In the case of resonance Raman Spectroscopy the energy of the incoming photon matches an energy transition so the electron is excited to a real energetic state.

$(v = 1)$ is the dominant Raman process in most cases. Figure 2.7.1 illustrates Rayleigh scattering, Stokes and anti-Stokes Raman scattering using a basic rovibrational energy diagram.

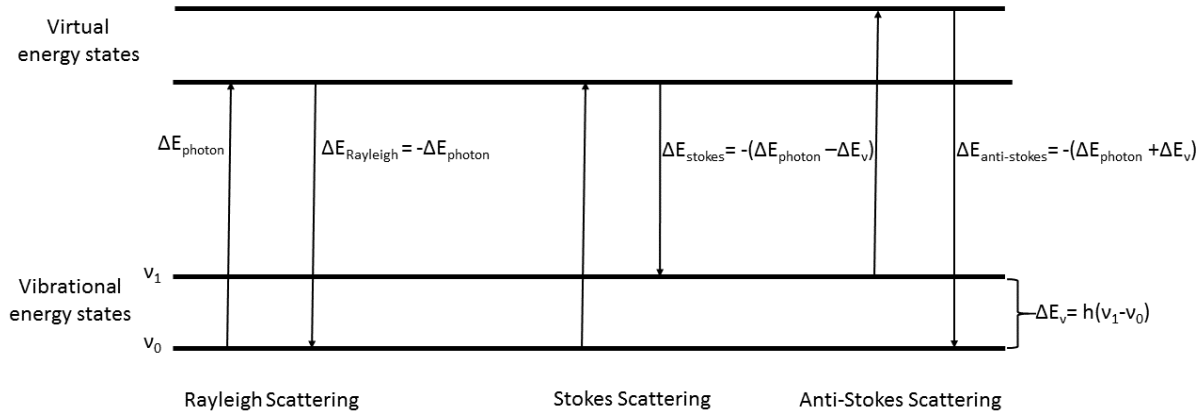

Figure 2.7.1: Energy diagram illustrating the vibrational energetic state transitions of a target molecule/crystal occurring in Rayleigh, Stokes and Anti-Stokes scattering.

A Raman microscope illuminates a target with a monochromatic laser and then measures the wavelength of scattered photons. The wavelength of photons which have been scattered through Stokes and Anti-Stokes processes are shifted, these processes are observed in a Raman spectra as a series of Raman peaks.

The Raman spectrum of graphene consists of 4 peaks which correspond to 4 separate Raman modes in the spectral region ~1200-2800 cm^{-1}. The peaks are labelled in a typical Raman spectrum of high defect density, monolayer graphene in Figure 2.7.2.

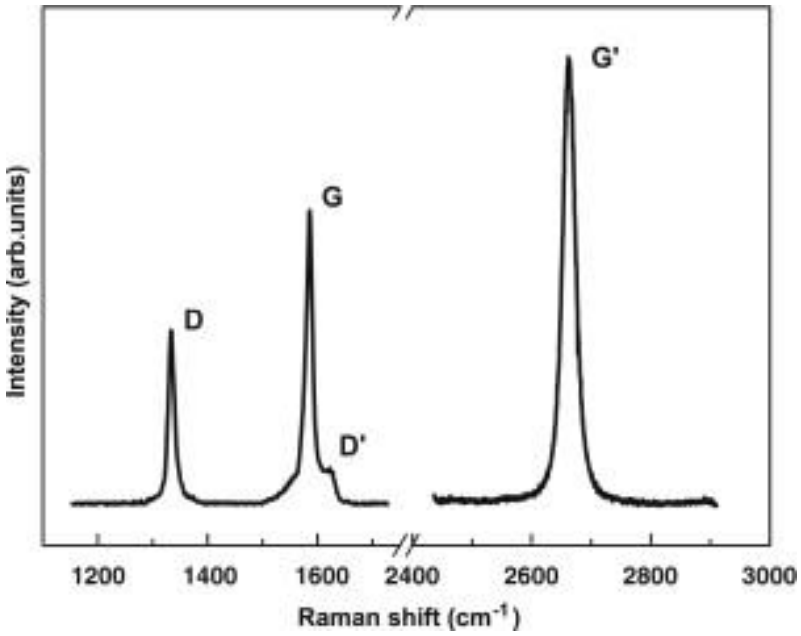

Figure 2.7.2: Raman spectra of monolayer graphene with Raman modes labelled.

The G peak is found around 1580 cm^{-1}, the 2D peak (otherwise known as G') at 2700 cm^{-1}. Two disorder-induced peaks D and D' are found around 1350 cm^{-1} and 1620 cm^{-1} respectively. The G mode is due to bond stretching of sp^2 carbon atom pairs, a first order Raman process, meaning it is mediated by a single phonon scattering event. The Raman processes responsible for the other peaks however are higher order.

The 2D and D modes are the result of 2nd order double resonance processes between electronic states at different corners of the Brillouin zone of graphene connected by 2 scattering events; 2 phonons for the 2D mode and a defect and a single phonon for the D mode. After photon mediated excitation, followed by two scattering events between 2 K-points in the BZ, electron-hole recombination occurs and a photon is emitted with a Raman shift characterised by the 2D and D modes. Figure 2.7.3 explains the Raman processes in terms of the energy dispersion relation around across the BZ.

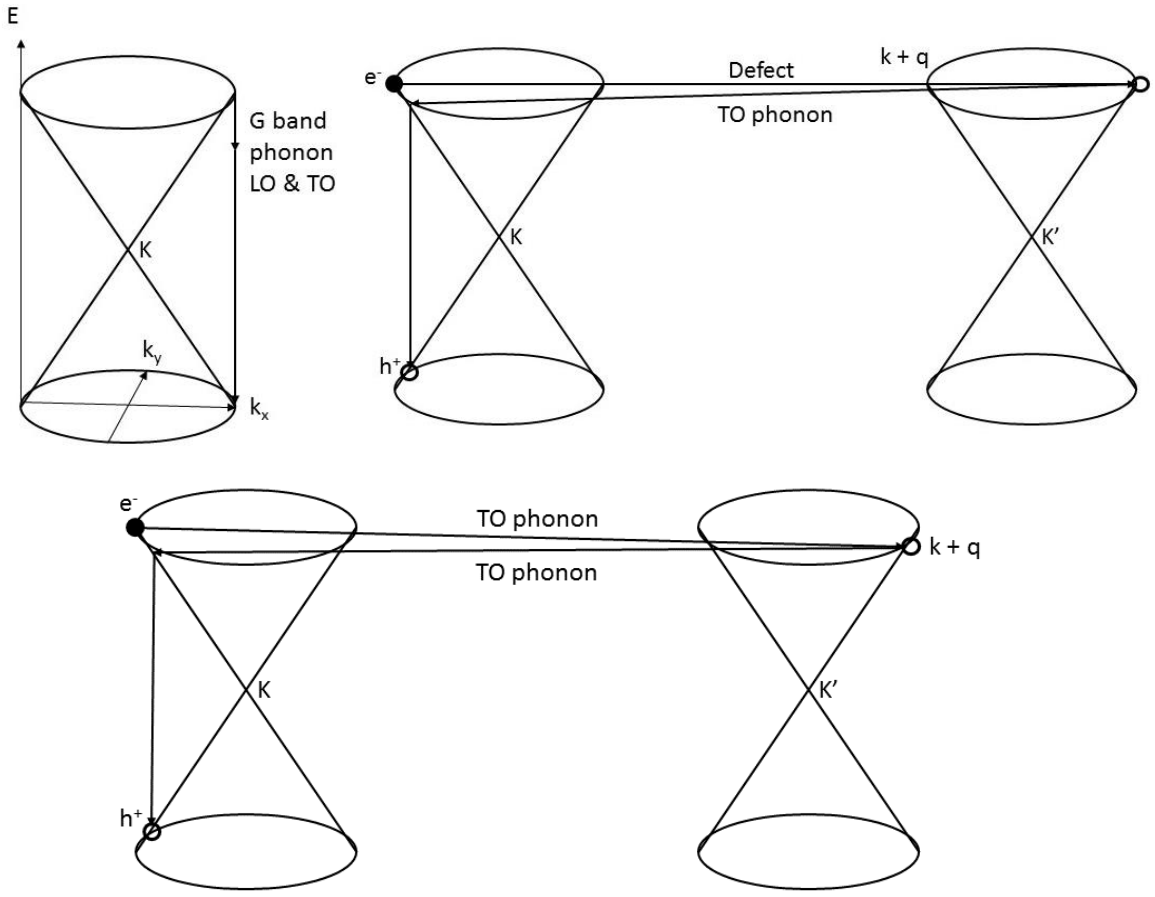

Figure 2.7.3: Energy diagrams showing the Raman processes responsible for the G, D and 2D peaks in monolayer graphene. The G process (top-left) is a first order Raman process and therefore is entirely situated near one corner of the BZ on a single side of an E-k valley. (top-right) and (bottom) represent the double resonant processes of the D and 2D Raman bands respectively. The open circles represent the resonant values of the wavevector q such that phonons couple with electronic states approximately the other side of an E-K valley near corners across the BZ.

Raman spectroscopy can be used to determine the number of layers in a graphene sample and the stacking order. As graphene increases in thickness, the 2D band splits into more phonon modes as out-of-plane phonon modes become active and electrons become affected by interlayer interactions [45]. The increase in the number of Raman modes responsible for the 2D peak, causes peak widening and reduction in intensity. Since in-plane phonons mediate the Raman process responsible for the G peak, the G peak intensity remains constant with increasing thickness. Graphene thickness may therefore be inferred through the G/2D peak ratios; ~0.5, 1 and 2 correspond to monolayer, bi-layer and tri-layer graphene respectively. Similarly, since the Raman process responsible for the D peak is defect mediated, the D/G peak intensity ratio increases with defect density. A study by [44] used low energy Ar^+ bombardment as a controlled means to introduce point-defects into monolayer graphene. By taking scanning tunnelling microscopy (STM) images to measure defect density, an empirical relationship between D/G peak intensity and defect density was found and is plotted Figure 2.7.4.

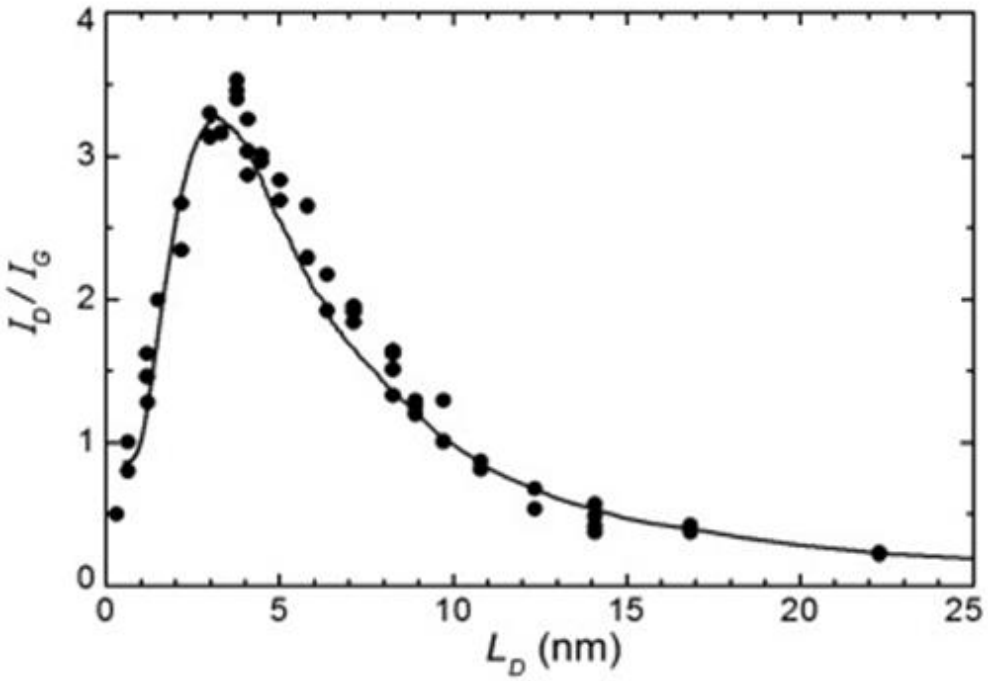

Figure 2.7.4: I_D:I_G intensity ratio vs inter-defect distance [44].

The relation between peak ratio and defect density plotted in Figure 2.7.4 is expressed below.

$$\left(I_D/I_G\right) = (102 \pm 2)/{L_D}^2. \qquad \text{Equation 2.7.1}$$

The above expression is only valid when $L_D > 5$ nm which is equivalent to $n_D < 4 \times 10^{11}$ cm^{-2}. At higher defect densities the in-plane phonons responsible for the D-band diminish, which leads to a decrease in the D/G peak intensity ratio.

Point Raman measurements are useful for quickly determining if there is graphene on a substrate and performing quick characterisation to find its thickness and approximate defect density. Furthermore, by taking an array of Raman measurements over an area of graphene, the defect density and thickness of a sample can be mapped over space. Large, high resolution Raman maps are used in this MPhil to determine the distribution of the defect density and thickness of graphene after CVD synthesis and Hall bar fabrication, providing statistical outputs which facilitate the discussion of using CVD graphene in heterostructure fabrication.

2.8 **Electrical Characterisation**

Factors such as defect density, domain size, doping and thickness has a profound impact upon the electrical properties of graphene. The most frequently referenced properties are sheet resistivity, charge carrier mobility and density. One aim of this MPhil is to provide a methodology which reliably produces specific architectures[12] of CVD graphene on Si/SiO_2 with repeatable electrical properties similar or better than that of typical commercially available CVD graphene on Si/SiO_2. The processing steps necessary in fabricating Hall bars from CVD graphene involve spin-coating polymers onto graphene, wet transfer, baking, etching, exposure to ions and impurities found in a laboratory environment and handling; each of these processes can potentially cause graphene degradation through defect formation, therefore this aim is by no means trivial. Additionally, fabricating graphene Hall bars will employ procedures which will be used in heterostructure fabrication (namely wet transfer and lithography) and therefore solutions to challenges which were met and overcome in Hall bar fabrication can be applied in the fabrication of heterostructures. Table 2.8.1 lists the quoted relevant electrical properties of commercially available graphene which was purchased from a commercial supplier[13] and characterised by myself in section 3.3 as well as the apparent monolayer coverage and maximum domain size.

[12] Hall bars are fabricated in this study as a specific architecture with features as small as 2 μm in size. Developing a methodology which reliably affords Hall bars can be applied in further work for heterostructure fabrication.
[13] Commercial graphene was purchased from www.graphenea.com

Table 2.8.1: Relevant electrical and physical properties of commercially available graphene purchased for characterisation by the author [69].

Property	**Value**
Sheet Resistance on Si/SiO_2 over 1 cm^2	460 ± 40 Ω/sq.
Field Effect Mobility	4000 cm^2/Vs
Hall Effect Mobility	2000 cm^2/Vs
Monolayer Coverage (on Cu)	> 98%
Domain Size	< 10 μm^2

In this MPhil the sheet resistance and monolayer coverage of commercial graphene was determined; characterisation studies to determine field effect/Hall effect mobility and domain size may be performed in future work after device fabrication using the procedure in this report. Each method is discussed in this section regardless.

2.8.1 Sheet Resistivity Measurements

Sheet resistivity is typically determined through 4-terminal measurements, using a linear arrangement of Ohmic contacts as shown in Figure 2.8.1 if possible.

A known current is supplied between contacts 1 and 4 in Figure 2.8.1, through either connecting a large resistor in series with a voltage source or by using a current source. The potential difference between contacts 2 and 3 is then measured with increasing current across contacts 1- 4. Providing the graphene between 2 and 3 shows Ohmic behaviour, the longitudinal resistance R and sheet resistivity R_S of the sample between contacts 2 and 3 can therefore be determined using equation 2.8.1 whilst eliminating contact resistances:

$$R = \frac{\Delta V_{23}}{\Delta I_{14}} = R_S \frac{L}{W}, \qquad \text{Equation 2.8.1}$$

where,

L is the length of the sample, and W is the width of the sample.

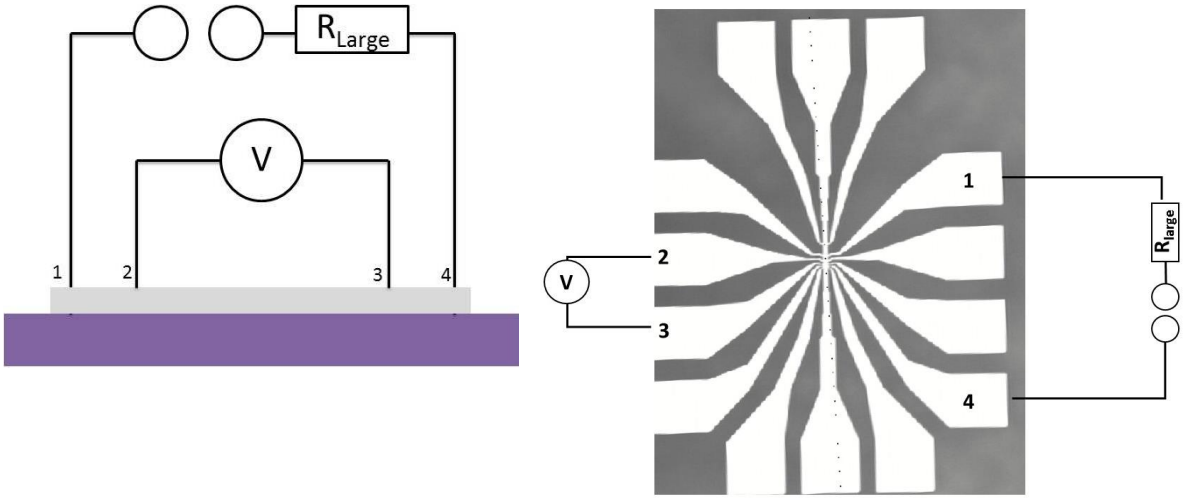

Figure 2.8.1. (top) Terminal set-up across a linear channel. (bottom) 4 point set-up using the optical mask used in this project (white and dark areas refer to conductive and insulting regions respectively) for hall bar fabrication as an example, the set-up acts a linear contact arrangement due to the central conducting hall channel.

Fabrication of graphene Hall bars enables the calculation of sheet resistivity using this simple 4 contact set-up. However, in cases where the sheet resistance of a graphene sample with an arbitrary geometry is being measured, the Van-Der Pauw technique is employed to determine the sheet resistance [46]. The technique is suitable for simply connected graphene sheets (no non-conducting domains) with arbitrary geometries. 4-contacts are made with the sheet ideally on the peripheries, a current is supplied across one pair and a voltage is measured across another as shown in Figure 2.8.2.

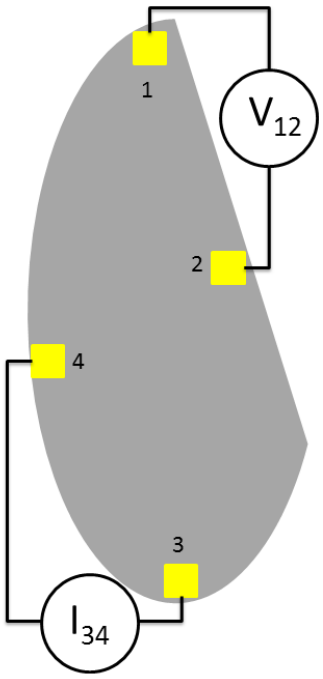

Figure 2.8.2. Diagram showing a typical Van-Der Pauw 4 contact measurement to determine one of the two resistances necessary to calculate R_S.

Two resistance terms are then measured by supplying current and measuring voltage across different contact pairs using the Equation 2.8.2 and Equation 2.8.3

$$R_A = \frac{\Delta V_{43}}{\Delta I_{12}} \qquad \text{Equation 2.8.2}$$

$$R_B = \frac{\Delta V_{14}}{\Delta I_{23}} \qquad \text{Equation 2.8.3}$$

The resistances are then input into Equation 2.8.4, which is solved numerically for the sheet resistance R_S. [71]

$$e^{\frac{-pR_A}{R_S}} + e^{\frac{-pR_B}{R_S}} = 1 \qquad \text{Equation 2.8.4}$$

2.9 **Hall Effect**

Any charged particle moving through a magnetic field, experiences a Lorentz force which is given,

$$\vec{F} = q\left(\vec{v}\times\vec{B}\right) \qquad \text{Equation 2.9.1}$$

where $\vec{v}\times\vec{B}$ is the vector cross product of the velocity of the charge and the magnetic field respectively.

In a Hall bar configuration, the Lorentz force causes electrons to build up on one side of the central conducting channel. The charge separation induces an electric field, $\overrightarrow{E_H}$ which exerts a force $\overrightarrow{F_H} = q\overrightarrow{E_H}$ upon charge carriers opposing the Lorrentz force so in equilibrium the following expression is true.

$$\vec{F} = q\left(\overrightarrow{E_H} + \vec{v}\times\vec{B}\right) = 0 \qquad \text{Equation 2.9.2}$$

The magnitude of the electric field at equilibrium is given by product of magnetic field, current density j_x, and the Hall coefficient R_H

$$\overrightarrow{E_H} = R_H\vec{B}\times\overrightarrow{J_x}. \qquad \text{Equation 2.9.3}$$

The Hall coefficient is an intrinsic material property, given,

$$R_H = \frac{\overrightarrow{E_H}}{\overrightarrow{B_z j_x}} = \frac{1}{ne} \qquad \text{Equation 2.9.4}$$

where n is the charge carrier density.

Hall bar measurements can be taken in order to find the charge carrier mobility and density of graphene. To perform Hall measurements, graphene Hall bars must be fabricated though lithography. The lithographic procedure is explained in detail in section 3.2. Figure 2.9.1 illustrates a typical Hall bar set up.

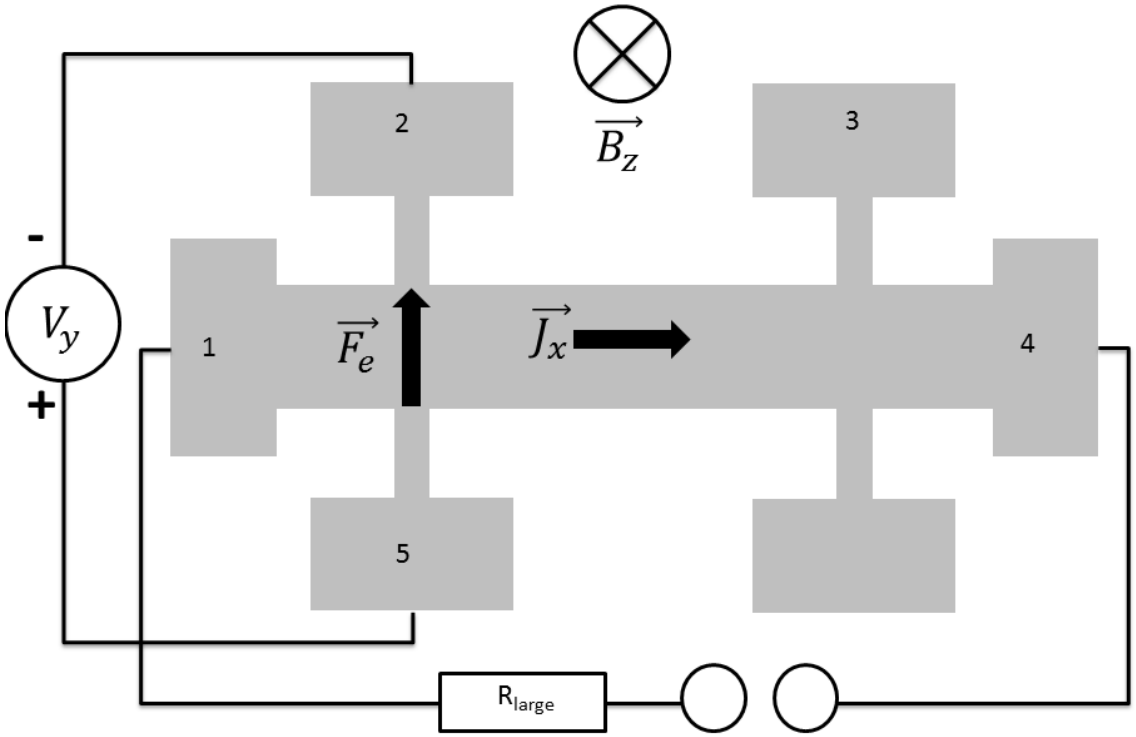

Figure 2.9.1: Hall bar set up where a current is applied between contacts labelled 1 and 4, a magnetic field $\vec{B}$ is applied into the page and the resulting potential difference is induced between contacts 2 and 5.

Typical Hall bar geometries for Hall measurement include a central conducting channel with a high aspect ratio and a series of side contacts which allow for 4-terminal resistance measurements. Using a lithographic mask, it is possible to fabricate large batches of Hall bars from a single CVD graphene sample, which enables high sample throughputs.

Considering the terms in Equation 2.9.4, the following terms are collected.

$$V_y = \frac{E_H}{W} \qquad \text{Equation 2.9.5}$$

$$j_x = \frac{I_x}{W} \qquad \text{Equation 2.9.6}$$

Thickness is omitted from the expression for current density as graphene is considered as a 2-dimensional system and therefore *n* refers to the sheet carrier density, the number of charge carriers per unit area. The following substitution is made such that charge carrier density may be determined using measurable parameters $V_y = V_{25}$ and $I_x = I_{14}$.

$$R_H = \frac{V_y}{I_x} = \frac{\overrightarrow{B_z}}{ne} \qquad \text{Equation 2.9.7}$$

$$n = \frac{B_z I_x}{e.V_y} = \frac{B_z}{e.\rho_{xy}}$$ Equation 2.9.8

where $\rho_{ij} = V_i/I_j$ is the Hall resistivity.

The Hall resistivity is related to the Hall conductivity σ_{xy} by the following tensor relation:

$$\sigma_{xy} = \frac{\rho_{xy}}{{\rho_{xy}}^2 + {\rho_{xx}}^2}$$ Equation 2.9.9

After determining the carrier density *n*, the carrier mobility can be found using the Drude formula (Equation 2.9.1 derived from the classical expression for Drude conductivity in Equation 2.9.10), and a 4-point sheet resistivity measurement:

$$j = \frac{ne^2\tau}{m_e} E = \sigma E$$ Equation 2.9.10

where *e*, τ and m_e represent the charge, mean free time and effective mass of a charge carrier.

$$\sigma = ne\mu_H$$ Equation 2.9.11

$$\rho_{xx} = \sigma^{-1} = \left(\frac{W}{L}\right)\left(\frac{V_{23}}{I_{14}}\right)$$ Equation 2.9.12

$$\mu = \frac{1}{\rho_{xx} ne} = \left(\frac{L}{W}\right)\left(\frac{I_{14}}{V_{23}}\right)\frac{e.V_{25}}{B_z I_{14}}\frac{1}{e} = \left(\frac{L}{W}\right)\left(\frac{V_{25}}{V_{23}}\right)\frac{1}{B_z}$$ Equation 2.9.13

The carrier mobility μ_H and carrier concentration *n*, are frequently used properties to characterise electronic quality of graphene samples.

2.10 Field Effect Measurements

The application of a perpendicular electric field to graphene *via* a back or top gate voltage in a set up, similar to one shown in Figure 2.10.1 allows control over the Fermi level of electrons in graphene and hence the Hall resistance.

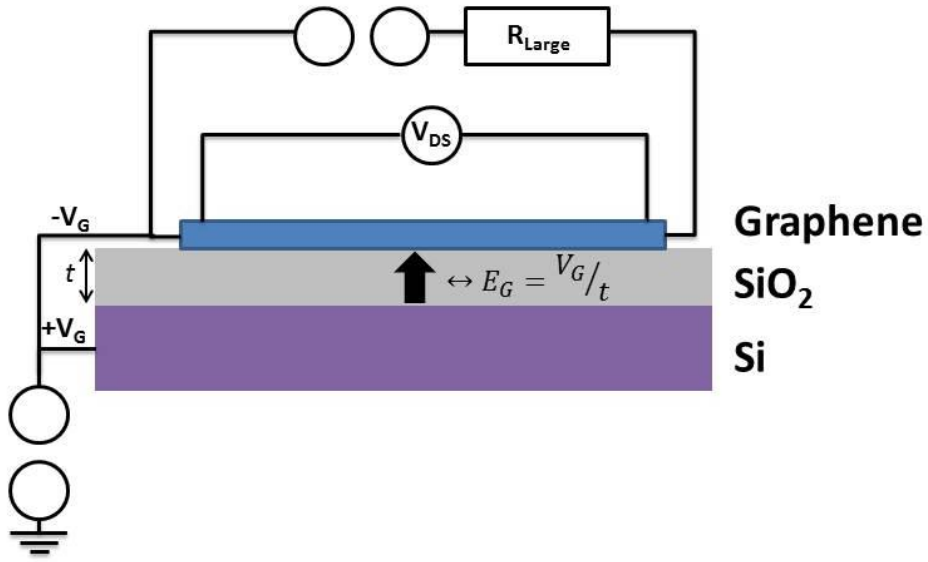

Figure 2.10.1: Set-up for field-effect measurements of graphene.

The oxide layer on the top of silicon substrates acts as an insulting gate. When a gate voltage is applied across the oxide layer, a perpendicular electric field induces surface charges at the oxide-graphene interface. Applying a gate voltage causes the Fermi level, E_F, of (undoped) graphene to shift away from Dirac point[14] at $V_g = 0$. By applying a positive gate voltage, E_F increases above the Dirac point into the CB and the number of charge carriers increases, such that electrons are the majority charge carriers. When $V_G < 0$, E_F is found in the VB, but the density of the majority charge carrier, in this case holes, increases. Charge doping from interactions between graphene and impurities/substrates causes the charge neutrality point to shift such that a finite gate voltage is applied to reach the charge neutrality point, identified in an R(V_g) plot as a maximum. If the graphene is p-doped, which it is often is after wet transfer due doping from PMMA residues, a positive gate voltage is required to increase the Fermi energy of graphene and reach the charge neutrality point. Gate field measurements can therefore be performed to determine how effectively PMMA residues are removed through post transfer treatment. Figure 2.10.2 compares typical gate field measurements of undoped graphene with measurements performed on CVD graphene by [68] before and after current. The charge neutrality point shifts from approximately +40V to -5V indicating that PMMA removal significantly reduces p-doping.

[14] The Dirac point is defined as the crossing point of the two linear dispersion bands of monolayer graphene, which, for undoped graphene is situated in k-space at the corners of BZ.

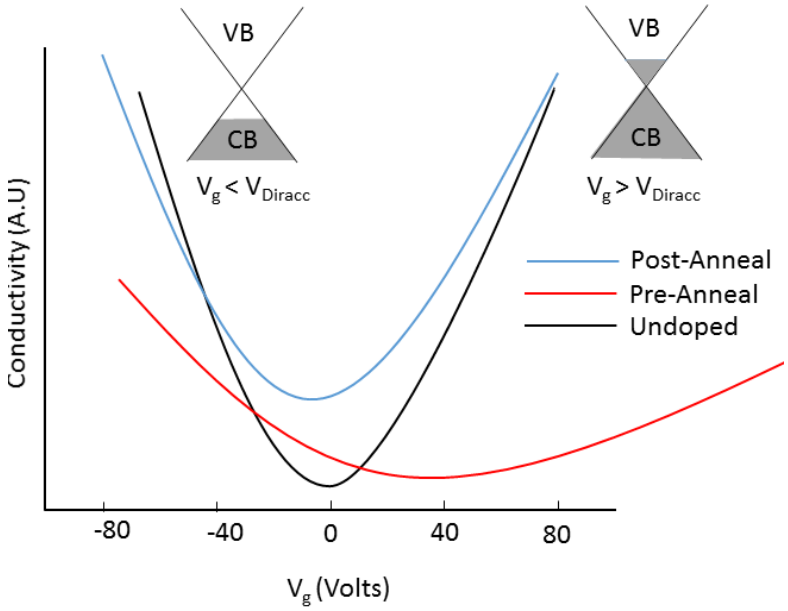

Figure 2.10.2: Plot of resistivity vs applied gate voltage for undoped monolayer graphene, and CVD graphene before and after current annealing, adapted from results by [68]. Energy dispersion cones diagrams are provided to illustrate how application of positive and negative gate voltages shifts the Fermi energy, E_F from the Dirac point into the conduction and valence band as shown in the energy dispersion cones.

Additionally, the gradient of the $\sigma(V_g)$ slopes increases significantly in Figure 2.10.2 after current annealing, corresponding to an increase in charge carrier mobility from 3200 $V^{-1}s^{-1}$ to 8000 $V^{-1}s^{-1}$: Modelling the oxide layer a simple capacitor, the induced carrier density, *n* through application of a gate voltage is approximated by

$$n = \frac{V_g \varepsilon_0 \varepsilon}{e.t} \qquad \text{Equation 2.10.1}$$

Where ε_0 is the permittivity of free space, ε is the relative permittivity and *t* is dielectric thickness.

2.11 **Negative Differential Resistance**

The simplest way to use Gr-Di-Gr heterostructures to measure pressure is to measure changes in a tunnelling current across the dielectric layer with a constant applied bias voltage as the dielectric layer is deformed through applying pressure. Since tunnelling current changes dramatically with sub-nm distances, tunnelling heterostructures show promise for highly sensitive pressure sensors employing this methodology. Whilst a purpose of this MPhil is to provide methodologies to fabricate Gr-Di-Gr heterostructure devices, it is important to discuss strain-dependant negative differential resistance (NDR) since this will likely be investigated after device fabrication in further studies.

Ohm's law is a linear relation which describes the voltage-current relation in components which exhibit Ohmic resistance. Non-Ohmic components such as diodes and capacitors exhibit other V-I relationships, including non-linear behaviour. Resonant tunnelling structures/devices, similar to the proposed Gr-Di-Gr heterostructure under development in this project, have been shown to exhibit non-Ohmic behaviour, specifically a negative differential resistance region. Gr-Di-Gr tunnelling heterostructures, illustrated in Figure 2.11.1.a, exhibit an NDR region for voltages immediately higher than a resonant peak in conductivity. As a bias voltage is applied between two graphene layers in a tunnelling heterostructure, an electric field is set-up across the dielectric which causes the Dirac points of the graphene electrodes to become misaligned by a wavevector *k*. The in-plane wavevector of an electron tunnelling from one electrode to the other must change by the misalignment, *k*. Therefore, electron tunnelling must be accompanied by a *–k* scattering process to satisfy momentum conservation laws. This selection rule limits the tunnelling current across the dielectric. However, application of a gate voltage across the heterostructure with the opposite polarity to the bias voltage can be applied to realign the Dirac points in reciprocal space. When applying finite gate voltages in a set-up like the illustration in Figure 2.11.1.a, resonant peaks in conductivity are observed during bias voltage sweeps when the Fermi-level chemical potentials are aligned through and therefore electron tunnelling is not restricted by scattering mediation to satisfy momentum conservation rules. Therefore, by applying a gate and bias voltage which changes the band alignment and chemical potential in the bottom graphene layer, a highly tuneable NDR region is controlled in tunnelling heterostructures. Figure 2.11.1.b shows tunnelling current – Bias voltage (V_B) curves measured across a Gr-hBN-Gr heterostructure fabricated in 2012 by Britnell *et al*, with a series of applied gate voltages [9]. By changing the gate voltage which is being applied, the

resonant peak changes position as the bias voltage necessary for non-scattering tunnelling is altered.

Previous studies by Littlejohn *et al* from the Nogaret group revealed that NDR measured across a graphitic nanoparticle composite (GNC) increases in peak voltage with strain [15]. Additionally, by connecting a GNC with a resonant circuit and applying a load voltage in the NDR region, oscillations in voltage across the GNC were observed with a strain dependant resonant frequency. Similar measurements will be performed using Gr-Di-Gr tunnelling heterostructures in order to use these devices to encode strain through frequency.

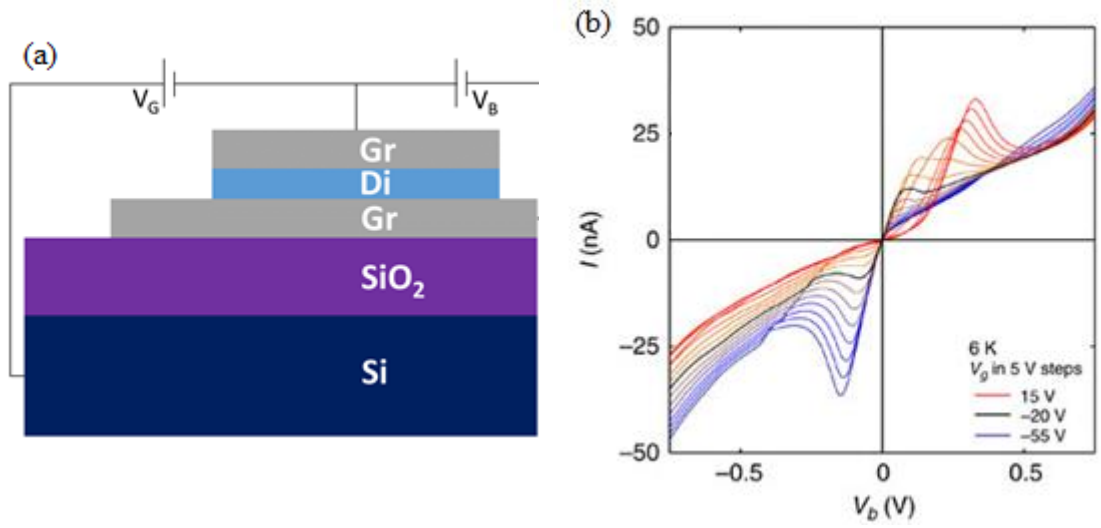

Figure 2.11.1: (left) Illustration of a Gr-Di-Gr Heterostructure with bias and gate voltages applied. **(right)** The I-V measurements across a graphene-hBN-graphene tunnelling capacitor with a series of applied gate voltages. The dielectric layer is 4 atomic layers thick [9].

3 Graphene Synthesis and Characterisation: Methodology and Results

3.1 Chemical Vapour Deposition

Graphene was grown on Cu substrates using the CVD methodology which was optimised as a collaborative effort between the author of this study and Andrew Rushworth of the Johnson Group. Raman maps of commercially available CVD and graphene synthesised *via* the procedure described in this section were collected and are compared in section 3.1.2.

3.1.1 Methodology

The optimised CVD steps for the particular set-up being used are shown below. Optimisation was performed by performing point Raman measurements on graphene on Cu after deposition to check the thickness and defect density. If the G/2D peak intensity ratio of a point spectra corresponded to bilayer or thicker graphene films, residence time and/or CH_4 pressure was reduced. Similarly, if the graphene Raman peaks were not detected, CH_4 pressure/residence time was increased. Optimisation steps towards the reduction of defect density were not as obvious, but instead based on a thorough literature review of the CVD growth of graphene[15].

1. Clean a large piece of 99.99% purity polished Cu foil in acetone, followed by de-ionised water and isopropanol cyclically 3 times. Dip in dilute nitric acid until all of the Cu surface starts bubbling. Rinse in de-ionised water then isopropanol. Dry using N_2 air.
2. Anneal the etched Cu in the CVD heating vessel at 1050 ˚C for 4 hours whilst constantly flowing 15 cm^3 $min^{-1}$of H_2 through the vessel and pumping.
3. Turn heat off, allow to cool down. Flow N_2 through the furnace for a faster cooling rate.
4. Cut the annealed copper into pieces as desired for graphene growth and heat the furnace to 1070 °C under a partial pressure of 1 mbar H_2 and 0.05 mbar CH_4. This ensures the methane flow stabilises before growing graphene. At this point the furnace must be positioned after the foil in terms of methane flow direction to avoid any graphene growth prior to reaching the correct temperature.

[15] Setting the annealing temperature of Cu to 1050 ˚C was the most significant input in the optimisation procedure by the author. Raman measurements were carried out by the author and Andrew Rushworth from the Chemistry Department.

5. When the furnace has reached 1070 °C, position it so it is directly heating the section of the reaction vessel containing the Cu foil.
6. After 15 minutes turn the methane flow off, turn the furnace off and allow to cool, using N_2 to speed up the process if necessary.

3.1.2 Surface Characterisation of graphene synthesised *via* CVD

Figures in this section provide Raman and AFM surface characterisation of a single sample of CVD grown graphene, obtained after CVD method optimisation. The Raman results are analysed and compared with commercially purchased CVD graphene to determine whether the CVD system described above could be successfully used in heterostructure fabrication, the AFM results provide an insight into how processing steps may affect the topography of graphene samples and therefore facilitate the discussion of methods which may help improve surface quality.

After depositing graphene on copper, initial point Raman measurements were performed to ensure there was graphene on the copper and it was the desired thickness prior to further processing or characterisation[16]. Initial point Raman measurements were also used as an initial test to determine whether the quality of graphene grown on Cu was adequate or whether further optimisation of the growth parameters was required.

The Raman spectra in Figure 3.1.1 show examples of the spectra which were observed in this study when performing point measurements on graphene synthesised by the CVD method described in section 3.1.1, and were considered adequate for further characterisation/device fabrication[17].

[16] During CVD method optimisation, these point measurements were performed by both the author and Andrew Rushworth. Andrew Rushworth used the data for further method optimisation.
[17] It is worth noting that a large number of graphene samples were used to destruction in the method development of Hall bar fabrication and it was not until this procedure was finally performed successfully that graphene grown by Andrew Rushworth was fully characterised by Raman mapping in this section.

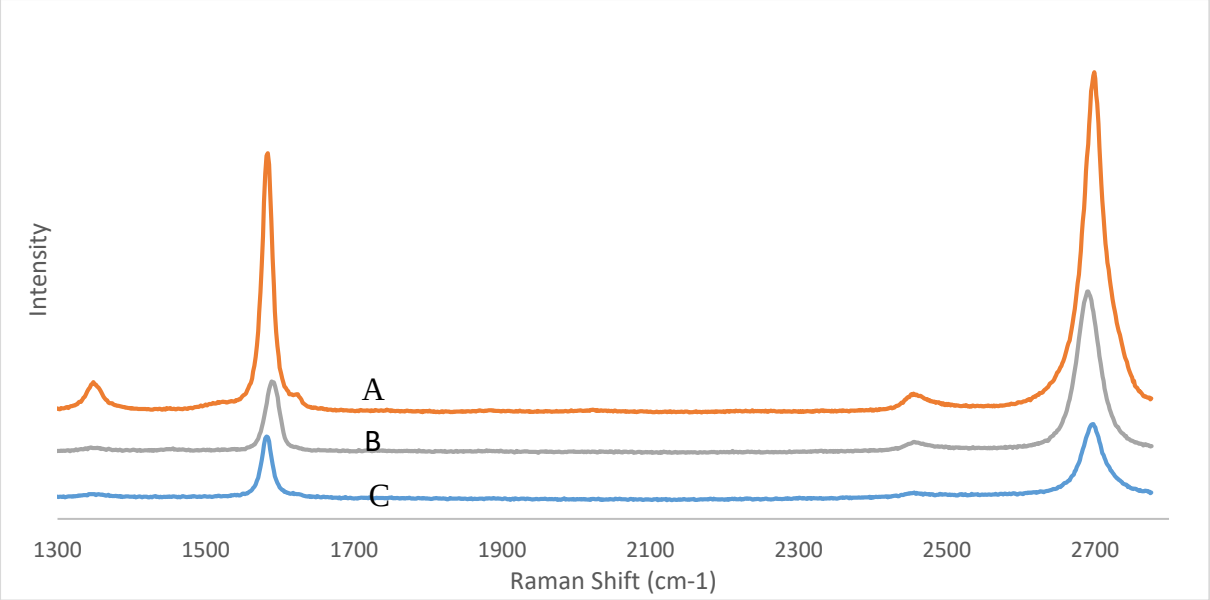

Figure 3.1.1: Three example Raman spectra of a single graphene on Cu sample taken at arbitrary positions (A-C from top to bottom) using a green wavelength (532nm), 10 second accumulations and a spot size of approximately 2 μm diameter.

The defect densities corresponding to each Raman spectra in Figure 3.1.1 was calculated using Equation 3.1.1 and input into Table 3.1.1.

Table 3.1.1: Peak ratios, approximate inter-defect distances and densities calculated using empirical equation, Equation 3.1.1

Spectra	I_D/I_G	L_D **(nm)**	N_D**(10⁹ cm⁻²)**	I_G/I_{2D}	**Number of layers**
A	0.106	31.0±0.3	10.4 ±0.2	0.77	1-2
B	0.046	47.0 ±0.4	4.53 ±0.1	0.44	1
C	0.064	39.9 ±0.4	6.28 ±0.1	0.84	1-2

Equation 3.1.1 allows the calculation of defect density using ratio of the D and G peak intensities for inter-defect distances (L_d) larger than 5 nm using [48] (meaning it is reliable for intensity ratios (I_D/I_G) less than 1.02):

$$\left(I_D/I_G\right) = (102 \pm 2)/{L_D}^2 \qquad \text{Equation 3.1.1}$$

Additionally, the number of graphene layers illuminated by each Raman spectra was determined and included in Table 3.1.1 using the following limits [45]:

Monolayer graphene:	$I_G/I_{G'} < 0.6$
1-2 layers:	$0.6 < I_G/I_{G'} < 1$
2-3 layers:	$1 < I_G/I_{G'} < 2$
More than 3 layers	$I_G/I_{G'} > 2$

Table **3.1.1** shows the inter-defect distance, defect density and thickness of the regions of graphene illuminated in each spectra in Figure 3.1.2. The peak ratios of spectra A and C show that the ~ 4 μm^2 regions illuminated by the Raman laser contain both monolayer and bilayer domain. This is caused by the growth of bilayer domains over monolayer graphene; studies have shown that bilayer domains grow over monolayer nucleation sites before monolayer films become continuous [67] therefore that the domain size of graphene over locations corresponding to spectra A and C is < 4 μm^2. Whilst the peak ratio of the Raman spectra B is not sufficient to determine whether the region of graphene illuminated is a single domain of graphene, the presence is bilayer domains is negligible, suggesting graphene domains are significantly larger.

Full Raman characterisation of a sample of graphene on copper grown by the optimised CVD method was performed once the Hall bars could be successfully produced[18] (Figure 3.1.2). D/G and G/2D Raman peak ratios were mapped over large areas of the sample for comparisons with commercially available graphene. Very large high resolution (~13 μm) Raman maps were produced to provide accurate statistical quantities of the sample, determine long range homogeneity and to provide data which could reveal more information about the CVD growth mechanism on Cu substrates.

[18] The intention was to fabricate Hall bars using the graphene which had been characterised *via* Raman spectroscopy

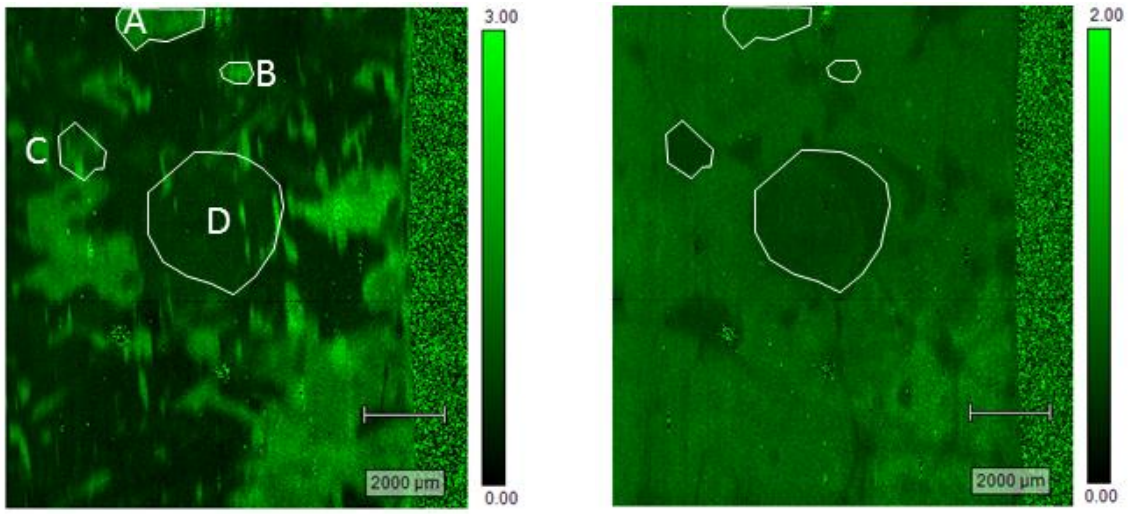

Figure 3.1.2: Maps of a graphene sample on copper approximately 11x12 mm in size showing the D/G which infers graphene thickness (left) and G/2D peak ratios which infers defect density (right) with scale bars and colour scales. Different contrasting regions are identified and labelled A-D for further analysis.

The D/G Raman peak ratio map shows the thickness coverage of the sample, i.e. bright areas represent a higher D/G ratio and therefore thicker areas of graphene. Statistical quantities such as average graphene thickness were calculated using these measurements and are shown in table 3.1.2. Similar analysis of the G/2D Raman peak ratio maps determined the statistical quantities referring to the average defect density of the graphene samples, which are also included in table 3.1.2.

Through inspection of the results shown in Figure 3.1.2, physical features of the samples may be observed, including the edge of the sample as a noisy region of the right-hand side of each map. Discontinuities in the graphene sample are observed as contrasting pixels or noisy regions; individual and small groups of pixels are scattered over the sample (approximately 5-10 groups per mm^2), a few larger tears and holes as large as ~400µm in diameter are also observed.

The maps in Figure 3.1.2 reveal that the graphene grown on Cu *via* the CVD method described in section 3.1.1 varies in thickness and defect density between different long range regions/domains. These domains can be seen clearly in both Raman maps as features ranging in size from ~100 µm to 2mm. The regions appear as areas with particularly contrasting defect densities and thickness; some regions which are clearly identified using one map may not be seen clearly in the other whereas other regions may be clearly identified in both maps. A selection of the different regions highlighted in Figure 3.1.2 were analysed to determine the amount the defect density and thickness distributions varied from region to region and the results being plotted in Figure 3.1.3 and Figure 3.1.4.

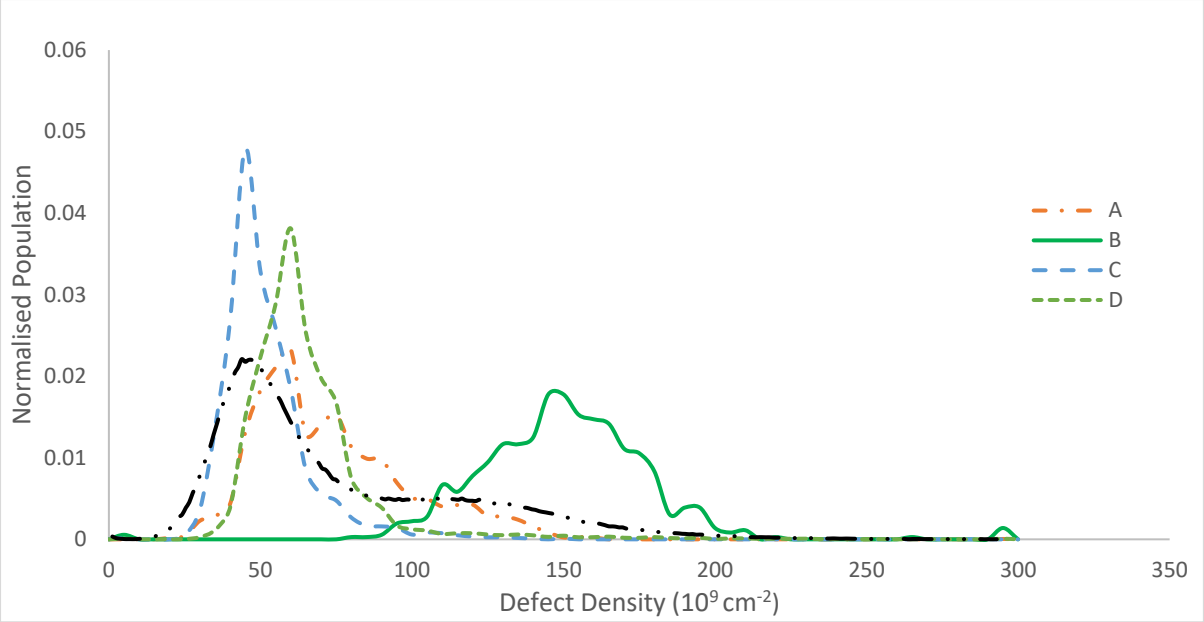

Figure 3.1.3: Normalised population[19] of Defect Density population of spectra within each region highlighted in the Raman maps in Figure 3.1.2 with a bin size of and the total population of the map (excluding regions not corresponding to graphene)

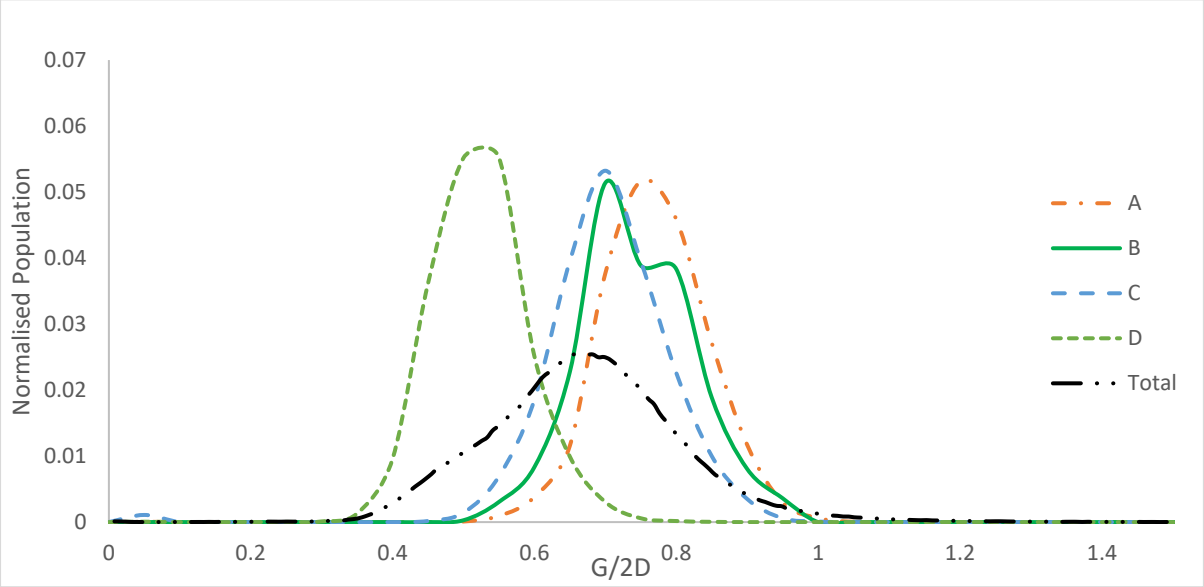

Figure 3.1.4: G/2D population of spectra within each region highlighted in the Raman maps in Figure 3.1.2 and the total population of the map (excluding regions not corresponding to graphene)

[19] Data shown in figures 3.1.3 and 3.1.4 are smoothed histograms with x-axis bin sizes of 5 $\times 10^7$ cm^{-2} and a total population of 1 to show how the defect density populations vary between samples and measurements.

Table 3.1.2: Data from Raman measurements in each of the regions highlighted in Figure 3.1.2. Coverage is given as a percentage of the total area of a graphene sample. i.e. Sum of total = 1.

Region	**A**	**B**	**C**	**D**	**Total**
Monolayer	2.41%	5.83%	13.52%	91.35%	28.81%
1-2 layers	94.63%	91.00%	84.56%	6.88%	69.45%
2-3 layers	0.023%	0%	0%	0.007%	1.43%
>3 layers	2.82%	3.19%	1.38%	1.74%	0.23%
Average Defect Density (10^9 cm^{-2})	71.07	147.54	49.55	63.27	75.81

Figure 3.1.3, Figure 3.1.4 and Table 3.1.2 demonstrate that CVD grown non-commercial graphene contains separate regions with significantly different defect densities and thicknesses (likely due to different bilayer island densities). The regions visible on each Raman map appear similar in morphology to Cu crystal grains (these regions are seen more easily on the D/G map). Previous studies have shown that the Cu (111) surface promotes the growth of larger graphene domains than Cu (001) due to a small lattice mismatch (~4%) between the hexagonal Cu (111) and graphene lattices [63] [64]. Fewer graphene domains correspond to lower defect densities, therefore the regions in the D/G Raman maps correspond to different surface terminations of the underlying copper substrate with separate graphene domain sizes. Domains observed in the G/2D Raman maps are likely caused by the variation in carbon species adsorption and dissociation energies on different copper Miller surfaces. Cu grain sizes are typically much smaller using commercially available graphene since the annealing step, employed in the non-commercial CVD process is omitted. High temperature annealing has been shown to increase Cu grain size up to 3.5 mm [62]. These results prompt further investigations[20].

Ideally the properties of CVD graphene used for heterostructure fabrication would be homogenous across areas as large as each graphene electrode for an appropriate level of control over tunnelling barrier distances and the quality and thickness of each graphene electrode. Commercially available graphene was characterised *via* Raman mapping for comparison with the CVD graphene produced by the Johnson group. Fewer data points were used since the purpose of this characterisation was simply to determine the defect density and thickness of the commercially available graphene. Three ~50x50 μm Raman maps were produced at different

[20] This work may not be directly related towards the aim of heterostructure fabrication. However through molecular dynamic studies and/or a combination of X-Ray diffraction and Raman mapping, it may be possible to determine relationships between Cu surface termination and defect density.

arbitrary locations of a sample of commercially available graphene to determine the homogeneity of the graphene. Statistical outputs of each mapped area are shown in Table 3.1.3.

Table 3.1.3: Properties of commercially available graphene on copper from Raman mapping at three different arbitrary areas and the CVD graphene produced by the CVD process optimised and grown in the Johnson Group.

Graphene thickness	**Area 1**	**Area 2**	**Area 3**	**Total**	**Johnson graphene sample**
Monolayer	93.3%	82.1%	90%	89.5%	28.50%
1-2 layers	4.4%	14.3%	8.6%	7.7%	68.12%
2-3 layers	0%	0%	2.9%	1.4%	1.61%
>3 layers	2.2%	3.6%	0%	1.4%	1.65%
Number of spectra	45	28	70	143	729,397

The defect peak did not appear in any spectra when mapping the commercially produced graphene, therefore the maximum defect density, 6.45×10^9 cm^{-2}, is approximated through inspecting the noise/G-signal ratio and using equation 3.1.1 from a high signal-noise ratio spectrum, shown in Figure 3.1.4.

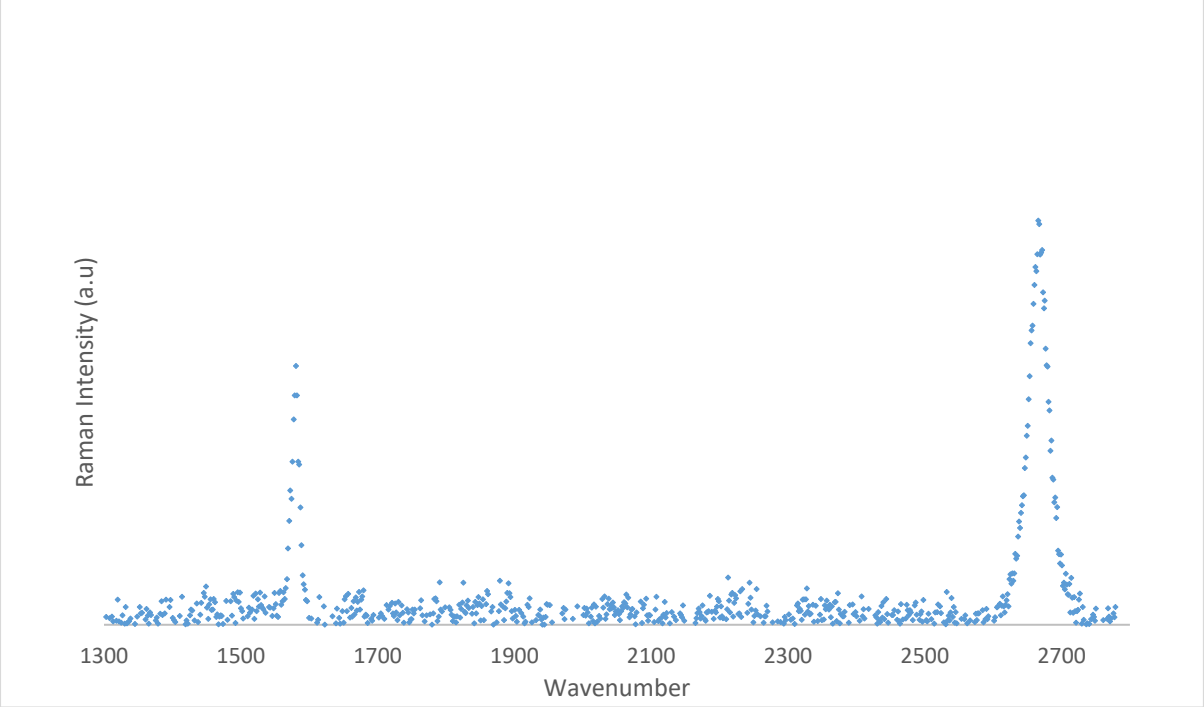

Figure 3.1.5: Typical Raman spectra of commercially available CVD graphene on Cu.

Raman mapping revealed that commercially purchased graphene has significantly higher monolayer coverage and lower defect densities than graphene produced in the CVD set up

described in section 3.1.1. This is likely due to the CVD rigs being used solely for graphene synthesis in industry and highly optimised growth parameters. It may seem obvious to use commercial graphene over the non-commercial CVD graphene characterised in this section for heterostructure fabrication, however the properties of CVD graphene degrade during wet-transfer and other processing steps. Cu substrate treatment procedures described in section 3.1.1 are not performed on commercial graphene, therefore a comparison between the properties of CVD graphene samples on Cu may not reflect the difference in properties after wet-transfer. Therefore, Raman and electrical characterisation of commercial and non-commercial graphene after device fabrication was also carried out in this MPhil in order determine how graphene should be sourced for heterostructures with optimum properties, with the results shown in section 3.2.2.

Whilst Raman measurements were vital towards this MPhil when determining properties such graphene thickness and defect density for surface characterisation studies, to fabricate graphene-dielectric-graphene heterostructures it is vital to be able to control the thickness of each layer being added. AFM measurements shown in Figure 3.1.6, were performed on graphene Hall bars to determine the surface roughness and step height of graphene on a Si/SiO_2 substrate post transfer and lithography. A linescan is shown in Figure 3.1.6 from bare substrate onto the graphene Hall bar; revealing a step height of ~1.2nm. To determine the average thickness of the graphene Hall bar, height statistics were taken over two regions, A and B. A difference of 1.21 nm was revealed ~0.82nm thicker than monolayer graphene. This difference can be accounted for by PMMA residues and graphene wrinkles.

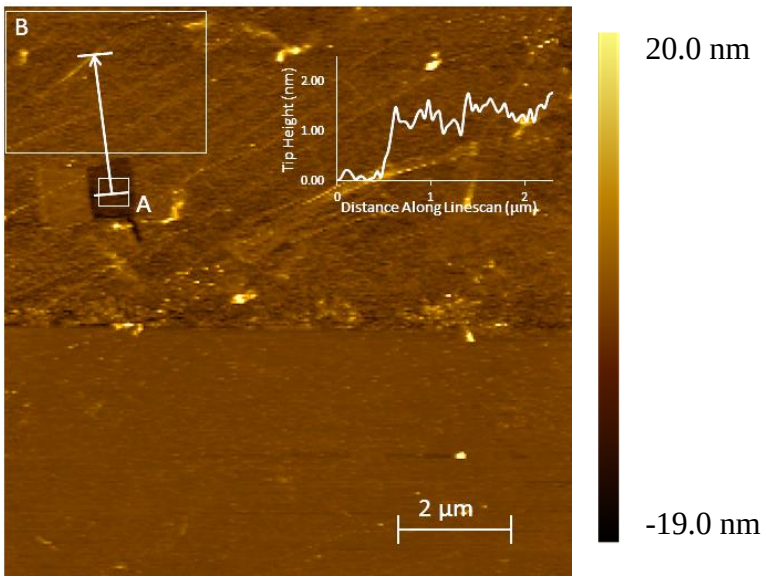

Figure 3.1.6: AFM image of a graphene Hall with no post-lithography treatment. An average of 15 adjacent linescans covering a width of 2.9 microns, denoted by the white arrow and end-scales, is included in the top of the image. The surface roughness of regions A and B were calculated as 0.22 nm and 2.48 nm respectively.

To determine whether the surface roughness and average thickness of graphene Hall bars could be reduced through PMMA removal methods, AFM measurements were taken on 2 graphene Hall bars from the same sample after treatment in chloroform for 24 hours and annealing at 300 ˚C for 2 hours. However, the AFM scans, shown in Figure 3.1.7 did not reveal any robust reduction in surface roughness or height through employing chemical treatment or annealing to remove residues. This is due to the variation in thickness and surface roughness of graphene between different areas of graphene caused by wrinkles.

Statistical quantities were determined within the regions denoted A, B and C in Figure 3.1.7 to determine how the topography of graphene changes depending on the number of wrinkles and are shown Table 3.1.4.

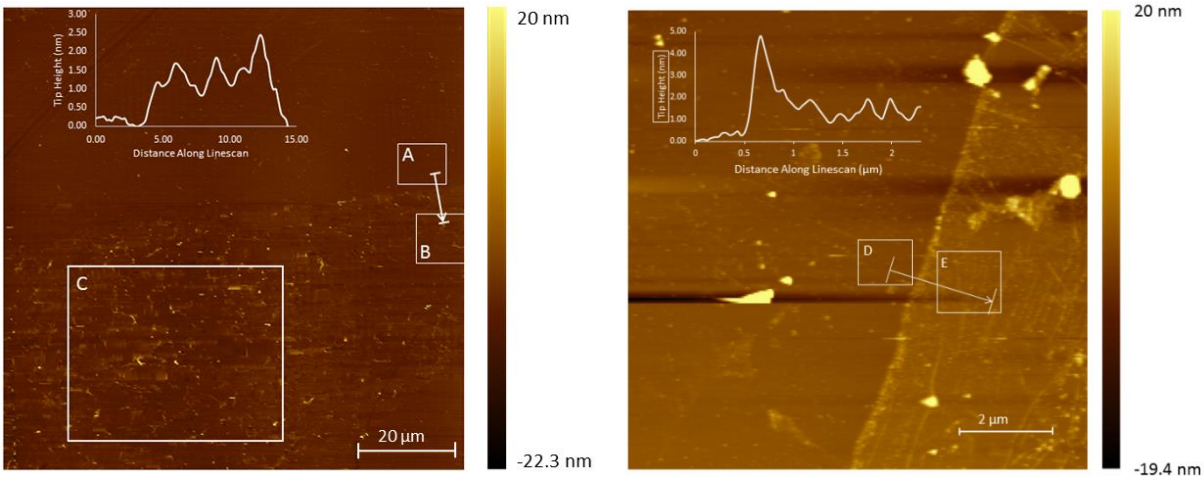

Figure 3.1.7: (Left) AFM scan of graphene Hall bar after wet chemical etching in chloroform for 24 hours to remove PMMA residues. An average of 15 adjacent linescans covering a width of 2.9 µm, denoted by the white arrow and end-scales, is included in the top of the image. A 0.8 µm moving average was used to smooth the linescan data. An average difference in height between regions A and B corresponded to a height of 0.87nm.

(Right) AFM scan of graphene Hall bar after annealing under vacuum at 300 ˚C for 2 hours. An average of 15 adjacent linescans covering a width of 0.6 microns, denoted by the white arrow and end-scales, is included in the top of the image. An average difference in height between regions D and E corresponded to a height of 1.44 nm; the surface roughness of graphene in region E was measured as 1nm.

Table 3.1.4: Statistical outputs of each region shown in Figure 3.1.7. Region A corresponds to bare Si substrate, B and C correspond to two regions of graphene, B containing less winkles than C. It is worth noting that whilst removal of polynomial backgrounds was performed using analysis software, a tip height drift of ~1nm over the map remained.

Region	**A**	**B**	**C**
Average Height (nm)	0.47	1.14	0
Maximum – Average Height (nm)	15.65	22.66	40.27
RMS Surface Roughness (nm)	0.70	1.76	3.15

A further AFM scan, shown in Figure 3.1.8, was performed on a non-wrinkled region of graphene after annealing under vacuum at 300 ˚C for 5 hours. This scan revealed that annealing is an effective technique to remove PMMA residues and minimise surface roughness of graphene.

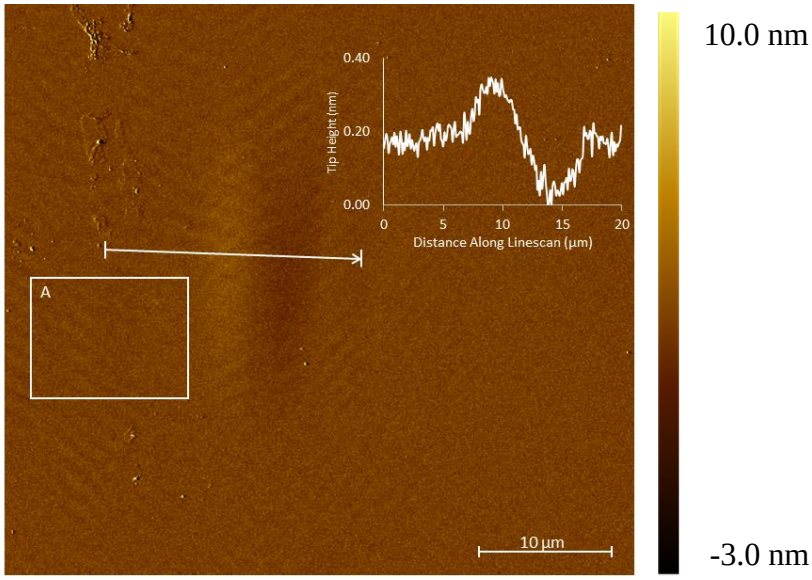

Figure 3.1.8: AFM image of a non wrinkled region of commercially available graphene after annealing under vacuum at 300 ˚C for 5 hours. An average of 15 adjacent linescans covering a width of 2.9 µm microns, denoted by the white arrow and end-scales, is included in the top of the image.

The surface roughness of region A is only 0.2 nm; over an order of magnitude lower than wrinkled regions. The linescan shows the profile of an unfolded wrinkle of graphene, which is only ~ 0.4 nm in height. Whilst fluctuations in height < 4nm in size, caused by graphene wrinkles, are undesirable since this limits the control over the thickness of a tunnelling barrier, the function of the tunnelling heterostructure will not be compromised by this variation. However, a small number of peaks, ~10s of nm in height were found on graphene post etching, likely due to remaining residues of PMMA or contaminants which have adhered to graphene after PMMA was removed by each process. Since the height of these features is greater than the desired heterostructure tunnelling barrier thickness, cleaning the graphene surface is necessary to avoid discontinuities forming in the tunnelling barrier. It is however worth noting that PMMA removal was not performed in a clean room, therefore it is worth repeating annealing and wet chemical treatment on graphene in a clean environment in order to see if contamination is avoided by doing so[21]. If contaminants remain an issue after annealing/wet etching in a clean environment, mechanical cleaning *via* rastering an AFM tip in contact mode remains a possible yet unfortunately quite time consuming solution. Previous work has

[21] These experiments are recommended as further work prior to heterostructure fabrication.

demonstrated that performing several AFM scans at a frequency of 0.5-2Hz removes all visible residues and causes a reduction in surface roughness of bilayer graphene on HbN from ~1nm to <0.2 nm [65]. If this technique is to be employed in the fabrication of graphene tunnelling heterostructures, the size of the heterostructures would be limited to the maximum AFM scan size (typically ~ 100 × 100 μm) and does somewhat limit industrial scalability.

A further Raman study was attempted to determine whether annealing and wet chemical treatment caused an increase in defect density, however due to the inhomogeneous distribution of wrinkles, which are major contributing factor in defect nucleation, the results were inconclusive.

3.2 **Contact and Hall Bar Fabrication**

3.2.1 Methodology

Graphene Hall bars were fabricated as a preliminary step to heterostructure fabrication to develop a procedure for successful lithography of graphene and Ohmic contact fabrication and to test the electrical properties of commercially available graphene.

The fabrication of micro-scale electronics often involves optical lithography which enables the transfer of a pattern onto a substrate. A substrate is covered by a photoresist, and then selected areas of the photoresist are exposed to UV light, locally changing the solubility of the photoresist. Development in an acidic solution dissolves the exposed areas of the photoresist for metal deposition. After deposition of a metallic film, typically by thermal evaporation or electron-beam evaporation, the remaining photoresist is dissolved in acetone, lifting the film off and leaving behind a metallic pattern on the substrate. It was found that lithography and deposition of Ohmic contacts must be performed prior to the transfer of graphene, elsewise graphene peels off the substrate in lift-off.

The following methodology was developed for the synthesis of graphene Hall bars and was performed using the commercially available CVD graphene characterised in section 3.1.2.

1. Silicon substrates with a 300nm thermal oxide layer are cleaned using acetone, DI water and isopropanol, followed by drying in N_2.
2. RF13 photoresist is spin-coated onto the substrate at 4000 rpm for 45 seconds.
3. The substrates are baked at 90 ˚C for 15 minutes.

4. The substrates are dipped in chlorobenzene for 2 minutes[22], followed by drying in N_2, not rinsing in DI water.
5. Substrates are baked for a further 15 minutes.
6. Edge beads are cut off using a scalpel to minimise any gaps between the substrate and mask, maximising the resolution of the lithography.
7. The contacts are brought into hard contact with the Ohmic contact pattern.
8. The samples are exposed 60 mJ cm^{-2} of UV light, this reduces the solubility of the exposed regions of the photoresist[23].
9. The samples are developed in a 5:2 developer solution for 45 seconds and immediately rinsed in water.
10. 20nm of Ti followed by 100nm of Au are evaporated onto the substrate.
11. The samples are heated in acetone at 60 ˚C with light irritation to lift off and expose the Ohmic contact pattern.

After depositing an Ohmic pattern onto Si/SiO_2 substrates *via* the method above, commercially available graphene characterised *via* Raman spectroscopy in section 3.1.2 was transferred onto the substrates using the wet-transfer procedure detailed below.

1. Spin-coat 4.6 g per $100ml^{-1}$, 480,000 g mol^{-1} PMMA dissolved in toluene onto the Cu-graphene sample at 4000 rpm for 45 seconds.
2. Bake at 110 °C for 15 minutes to stabilise the PMMA layer.
3. Float the Cu-graphene-PMMA stack in 1:1 HNO_3:DI water in order to etch graphene on the underside of Cu. When the Cu substrate starts to bubble, immediately quench in DI water.
4. Float the Cu-graphene-PMMA stack in 5g per 100 ml^{-1} $Na_2S_2O_8$ to dissolve the Cu[24].
5. Clean the graphene-PMMA film by washing with DI water, using a syringe 10 times. Wash 10 times with 5% HCl, then wash again with DI water repeatedly until the solution is a neutral PH, testing using litmus paper.
6. Scoop the graphene-PMMA film with a substrate by lifting at an angle to the film.

[22] Chlorobenzene hardens the top layer of a photoresist; therefore the lower layers of the photoresist develop quicker than the top, promoting undercut formation at the edges of patterned regions. This helps improve the precision of lift off [49].
[23] UV exposure is provided in total energy exposed rather than intensity since the UV lamp intensity reduces over its lifetime.
[24] Higher concentrations cause Cu to dissolve too quickly such that bubbles form which damage graphene.

7. Leave the substrate-graphene-PMMA stack to dry at an angle.
8. Bake at 110 °C for 30 minutes to improve the graphene-substrate adhesion.
9. Allow to cool.
10. Dissolve the PMMA in an acetone bath.

After transferring graphene onto the pre-patterned Si/SiO_2 substrate another lithographic process is undertaken in order to etch the graphene into continuous Hall bar architectures connected to the Ohmic contacts. The process does not involve lift-off; therefore, the chlorobenzene step is not necessary. The premise of this lithographic step is to leave photoresist on the graphene in the Hall bar pattern as an insulating layer. Then, *via* plasma etching and washing in acetone, graphene is left on the substrate in the Hall bar pattern. The steps below detail the process which was performed after commercially available graphene was transferred onto the pre-patterned contacts.

1. Samples are cleaned using acetone, DI water and isopropanol, followed by drying in N_2.
2. RF13 photoresist is spin-coated onto the substrates at 4000 rpm for 45 seconds.
3. The samples are baked at 90 °C for 30 minutes.
4. Edge beads are cut off using a scalpel.
5. The contacts are brought into close contact with the Hall bar pattern on the mask.
6. The samples are exposed 60 mJ cm^{-2} of UV light.
7. The samples are developed in a 5:2 developer solution for 45 seconds and immediately rinsed in water.
8. The samples are etched in an ICP-80 etcher using O2 Plasma with the following parameters - 250 W RF power, 200 W Forward Power, 25 scp O_2 flow rate, etch time 1 min.
9. The samples are rinsed in acetone and cleaned using DI water and isopropanol.

After Hall bars were fabricated, AFM, Raman and electrical characterisation was performed in order to determine whether commercially available graphene was suitable for heterostructure fabrication post transfer and lithographic processing.

3.2.2 Results

Table 3.2.1 lists the attempts to fabricate Hall bars and describes the challenges which were encountered and the way they were resolved. This table demonstrates how the processing procedures were adjusted over time until Hall bars were successfully fabricated and the methodology described in section 3.2.1 was reached.

Table 3.2.1: Lists some of the major challenges which were encountered in the fabrication process of graphene Hall bars and how they were resolved.

Problem	**Conditions**	**Attempted Resolution**
Overdeveloped photoresist	60 mJcm^2 UV exposure, 90 seconds development in 3.5:1 (water:developer solution).	Development time was reduced in 15 s steps from 90s until samples were no longer overdeveloped (at 30 s).
Poor lithography resolution	60 mj/cm^2 UV exposure, 30 seconds development in 3.5:1 (water:dev solution).	Likely caused by poor contact between mask and substrate, increase contact pressure, clean mask more thoroughly and use scalpel to remove edge beads of photoresist.
Contacts were not stable after lift-off. They peeled off when wire bonding.	Lithography conditions identical as above. Evaporation 12 nm Ti deposited at 0.5-0.7 nm/s,100 nm Au at 0.5-0.7 nm/s.	Attempted to resolve this problem by increasing the thickness of Ti deposited to improve the adhesion between graphene and the metal contacts.
Contacts were not stable after lift-off. They peeled off when wire bonding.	Lithography conditions identical as above. Evaporation 33 nm Ti deposited at 0.5-0.7 nm/s,98.5 nm Au at 0.5-0.7 nm/s.	Rather than sonicating to achieve lift-off, leave in acetone overnight with no irritation to avoid damaging contacts.
Contacts were not stable after lift-off. They peeled off when wire bonding.	Very similar conditions as above but using a gentler lift-off technique.	Thermal stress between contacts and graphene causes tearing as shown in Figure 3.2.1 so reduce deposition rate by a factor of 10 to reduce the temperature gradient across the metal-graphene interface.
Improved lift off, but still contacts peeled off when wire bonding.	Very similar conditions as above but deposition rates between 0.03-0.05 nm/s.	Evaporate metal contacts on substrate prior to graphene transfer.
Successful wire bonding, however the graphene Hall bars were not continuous.	Very similar conditions as above but arbitrary deposition rates.	Use a different technique to dice the sample prior to mounting in a chip package which does not involve touching the graphene.

As described in Table 3.2.1, a major issue which was faced was the deposition of metal contacts. Initial attempts to fabricate Ohmic contacts involved thermal deposition of Ti/Au

directly on graphene on Si/SiO_2. However, stresses caused by thermal contraction of the metal after deposition weakened the adhesion between graphene and the substrate underneath the contacts. Thus, exclusively on graphene regions, contacts peeled off the substrate along with graphene readily as shown in Figure 3.2.1a. The use of much slower deposition rates improved lift-off, however the adhesion between graphene the SiO_2 was still too weak for wire bonding. Instead, prior to wet transfer, substrates were prepared by evaporating metallic contacts directly onto the Si/SiO_2, shown in Figure 3.2.1b

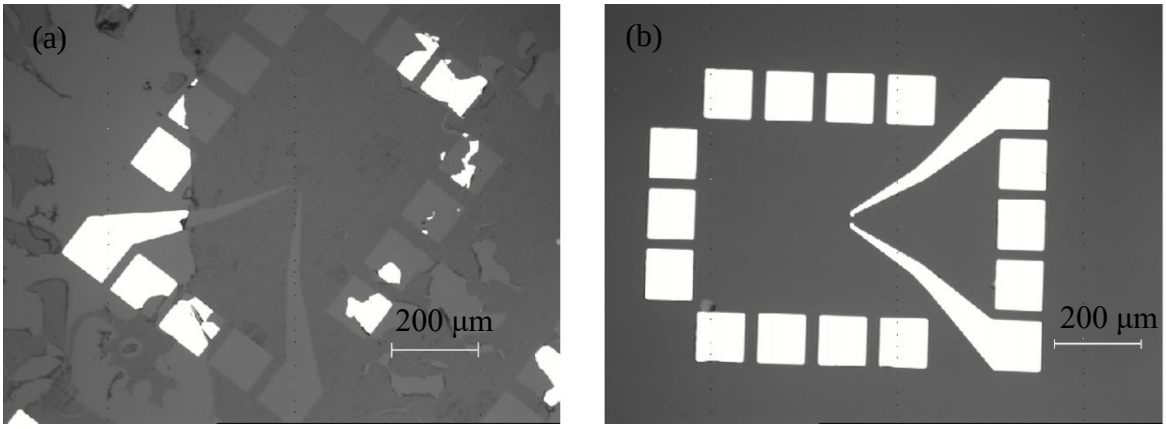

Figure 3.2.1: (a) Ohmic contacts evaporated on graphene-Si/SiO_2. Graphene can be seen as darker grey regions and bare silicon substrate is lighter grey. The microscope image was taken at the edge of a graphene region to demonstrate how the contacts peel off exclusively on graphene regions. (b) Ohmic contacts evaporated on Si/SiO_2.

After the methodology described in section 3.2.1 was optimised, Hall bars were fabricated using commercially available graphene. Lithography of features with a resolution of 2 microns was achieved, as shown in Figure 3.2.2.

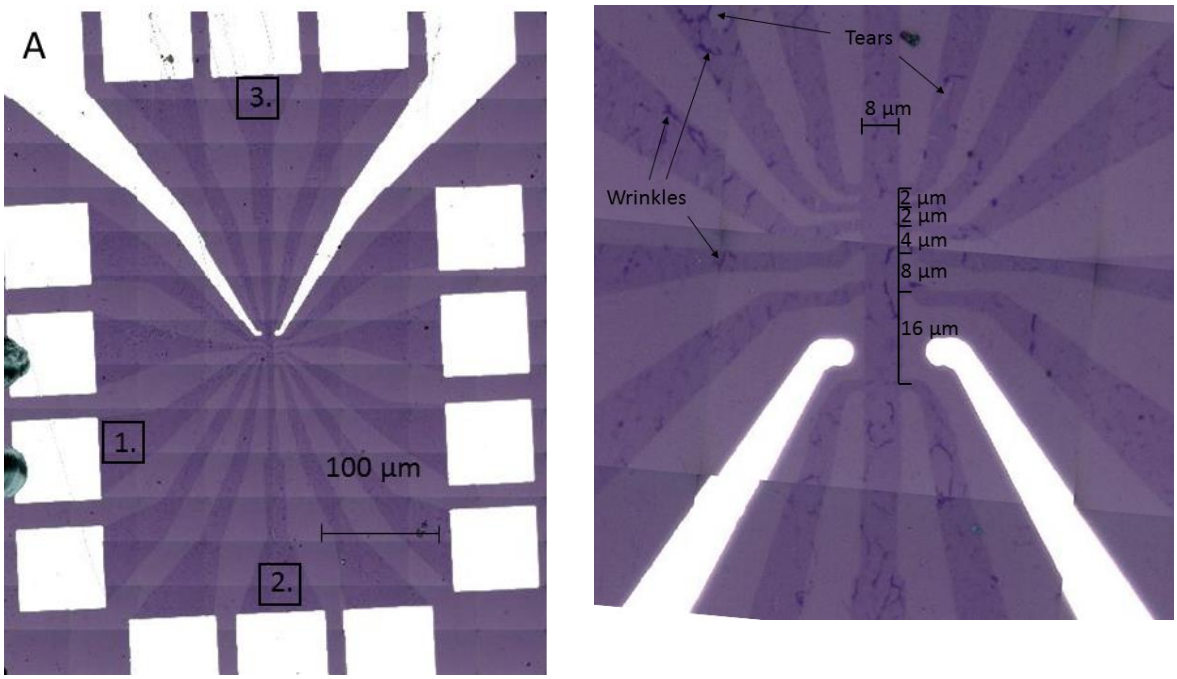

Figure 3.2.2: (A) Graphene Hall bar devices processed from commercial graphene showing the entire cell connected to ohmic contacts. (B) the dimensions Hall bars with an 8 micron wide Hall channel at a higher zoom. Tears and wrinkles are annotated, these features often arise after wet transfer.

Figure 3.2.2 shows two graphene Hall bar devices which were fabricated using commercial graphene. Whilst tears and wrinkles can be clearly seen, especially at the higher zoomed optical image, the graphene devices are clearly continuous and should conduct. After testing that Hall bars did in fact conduct using 2 contact measurements on a probe station, AFM, Raman and electrical characterisation was performed on Hall bars.

Raman mapping was performed on the two graphene Hall bars cells, A and B, shown in Figure 3.2.2 from the same commercially available CVD graphene sample to determine the extent of graphene degradation after wet-transfer and processing. D/G and G/2D peak ratios were mapped over 3 ~ 50 x 50 µm areas on each Hall bar device A and B. The areas mapped on Hall bar device A are highlighted in Figure 3.2.2, areas over similar locations were mapped on Hall bar device B. Table 3.2.2 lists some properties of graphene determined from each G/2D and D/G peak ratio map of each cell.

Table 3.2.2: Thickness and defect density of graphene Hall bars A and B from the same piece of commercially available graphene.

	A.1	**A.2**	**A.3**	**B.1**	**B.2**	**B.3**	**Total**
Monolayer Coverage	28.0%	2.1%	5.1%	18.2%	5.8%	10.2%	8.2%
1-2 layers	55.3%	70.8%	70.4%	83.6%	74.2%	64.8%	64.7%
2-3 layers	7.6%	23.6%	19.4%	9.1%	12.5%	19.4%	14.1%
>3 layers	9.1%	3.5%	5.1%	5.5%	7.5%	5.6%	5.6%
Average Defect Density (10^9 cm^{-2})	27.45	20.54	23.90	13.73	22.49	23.41	20.29
Sample Size	132	144	99	110	120	108	713

Table 3.2.2 shows that the average defect density of commercially available graphene increased more than threefold from less than 6.45×10^9 cm^{-2} before wet transfer to ~ 20.29×10^9 cm^{-2} after wet transfer. The defect density and thickness distribution of graphene was found to vary significantly between different regions post transfer; this is likely due to a non-homogeneous distribution of graphene wrinkles. Wrinkles form in graphene during wet transfer if there are gaps in-between the graphene sheet and the substrate when scooping. As the graphene dries and adheres to the substrate, tension causes graphene to protrude from the surface with a theoretical maximum in height of ~4nm [66]. If thermodynamically unstable graphene protrusions collapse, folding over themselves and forming wrinkles, defect density and number of layers, increases locally. This increase in mean and variation of thickness is observed in Figure 3.2.3 which compares the G/2D peak intensity ratio population distribution of commercial graphene before and after wet transfer and Hall bar fabrication. Before transfer bilayer and thicker regions of graphene are negligible as very few spectra with a G/2D peak intensity ratio over ~0.7 were measured. However, after transfer the average G/2D peak ratio remains significant for values up to ~ 1.6 which corresponds to mixtures of bilayer and trilayer graphene domains.

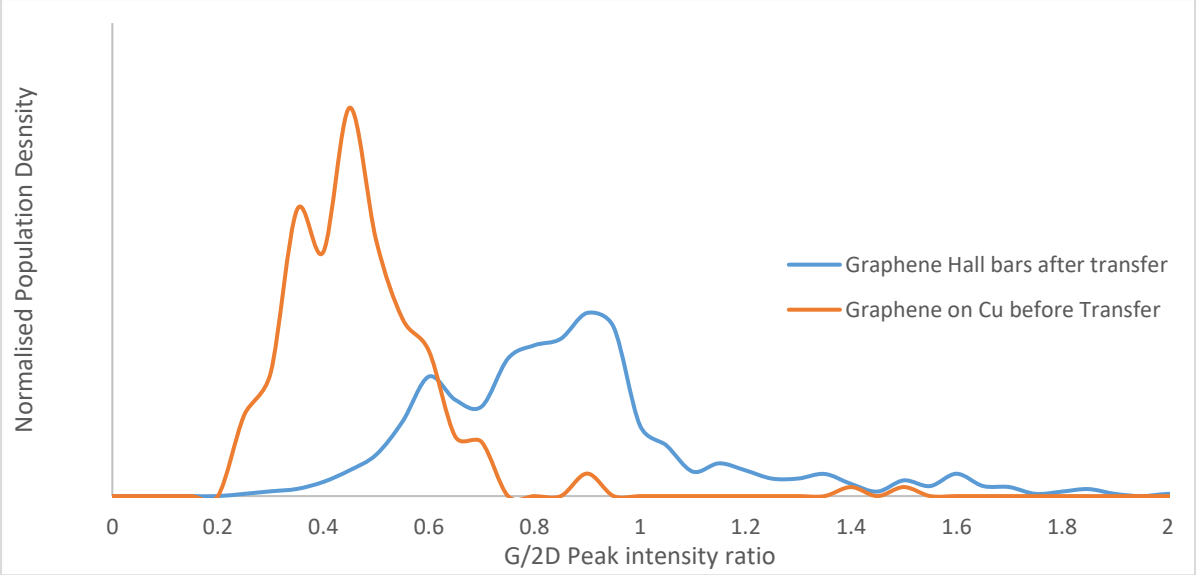

Figure 3.2.3: Averaged population distribution of G/2D peak intensity ratios from Raman maps taken over different areas of graphene on Cu prior to processing and on Si/SiO_2 post Hall bar fabrication.

Upon inspection under an optical microscope, wrinkles were present in the graphene samples after wet-transfer. Raman maps of the D/G and G/2D peak ratios were collected at the highest resolution available using the Raman microscope at the University of Bath (2µm) and the results compared with an optical image of the areas of graphene being mapped to determine the local effect of wrinkles upon the defect density and thickness graphene, (Figure 3.2.4).

The shape and size of wrinkles which can be seen in the optical image of graphene in Figure 3.2.3, matches the distribution of high intensity regions in the corresponding D/G and G/2D Raman peak intensity maps. The contrast in defect densities of wrinkled and non-wrinkled regions of graphene is shown as a peak and two plateaus in a D/G population distribution plot shown in Figure 3.2.4. The sharp population peak at lower D/G ratios represents areas not directly corresponding to visible wrinkles. It is worth noting that the defect density of commercial graphene in these regions has however still increased from $< 6.45 \times 10^9$ cm^{-2} to values between 8×10^9 cm^{-2} and 11.7×10^9 cm^{-2}, showing that defects are introduced to graphene in the transfer and lithography process irrespective of wrinkle formation; this is likely due to contaminants such as PMMA/photoresist residues, ions from etching the Cu substrate. The defect density of wrinkled areas of graphene reach values from between 2×10^{10} cm^{-2} and 6×10^{10} cm^{-2}.

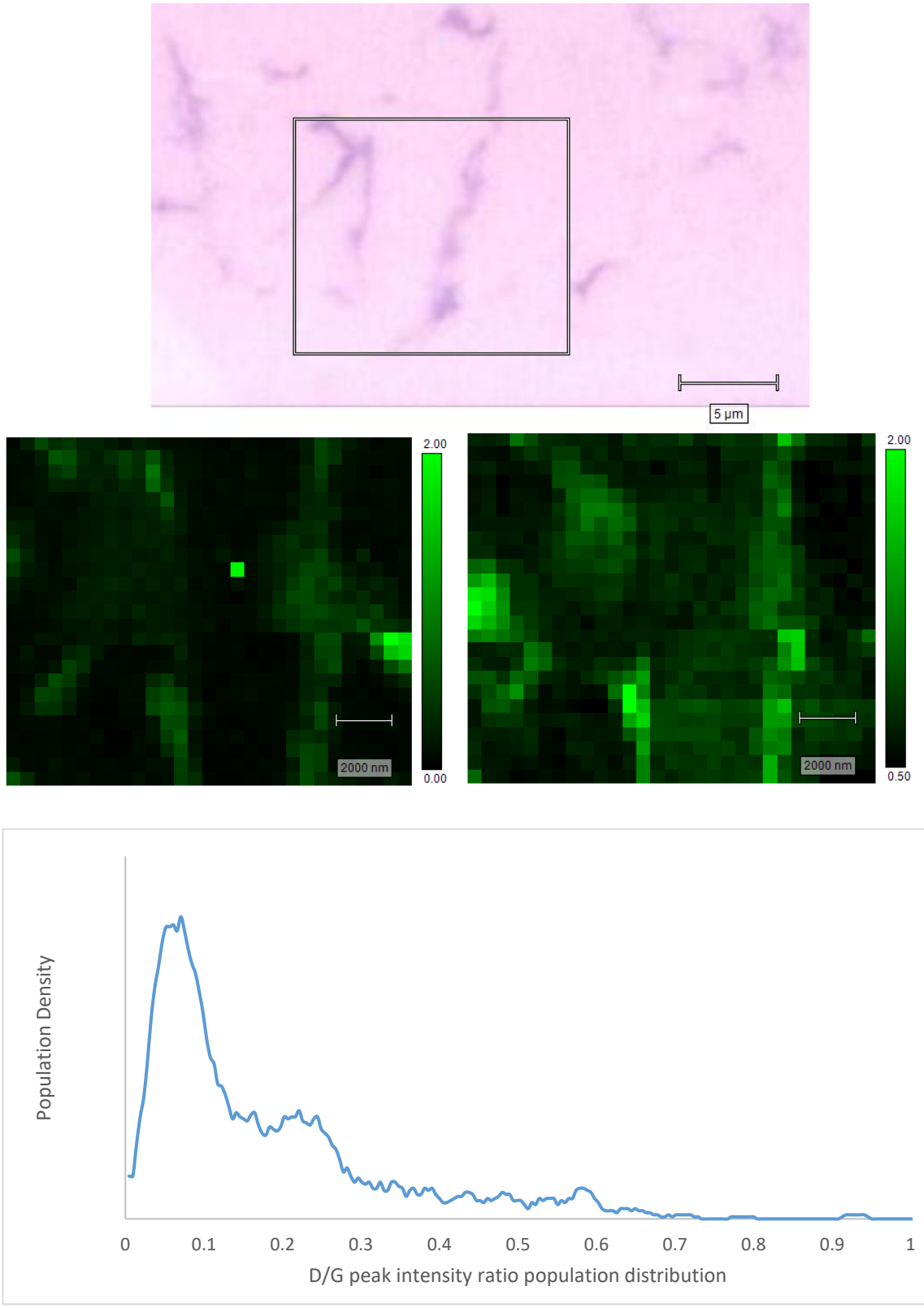

Figure 3.2.4: (Top) Optical image of wrinkles on graphene after transfer and fabrication of Hall bars with a box highlighting the area Raman mapped. (Middle-left) D/G peak intensity ratio map including a colour scale-bar. (Middle-right) G/2D peak intensity ratio map including a colour scale-bar. The pixel size (0.5 µm) in these maps was selected to be smaller than the spot size of the green Raman laser (~2 µm) to increase the data points for statistical outputs. (Bottom) Moving average D/G peak intensity ratio population distribution of the mapped wrinkled area of graphene above with a period of 0.015.

3.3 **Electrical Characterisation: Results**

After the procedure for Hall bar fabrication was set-up and Hall bars were fabricated successfully, electrical measurements were taken using the same transferred graphene samples characterised in the previous section. 2 contact measurements between Ohmic contacts were performed using a probe station to determine which Hall channels were continuous and conducted. On average 70% of the graphene Hall channels were continuous. Once it was established which contacts conducted, a current source was connected across either the central Hall channel or contacts as close to the central Hall channel as possible[25]. I-V measurements were then taken with voltage being measured across different contact pairs in order to plot longitudinal resistance against inter-contact distance to accurately determine sheet resistance. Figure 3.3.1 shows an I-V measurement across 2 graphene Hall bars with an aspect ratio of 1:4 from 2 samples which were characterised.

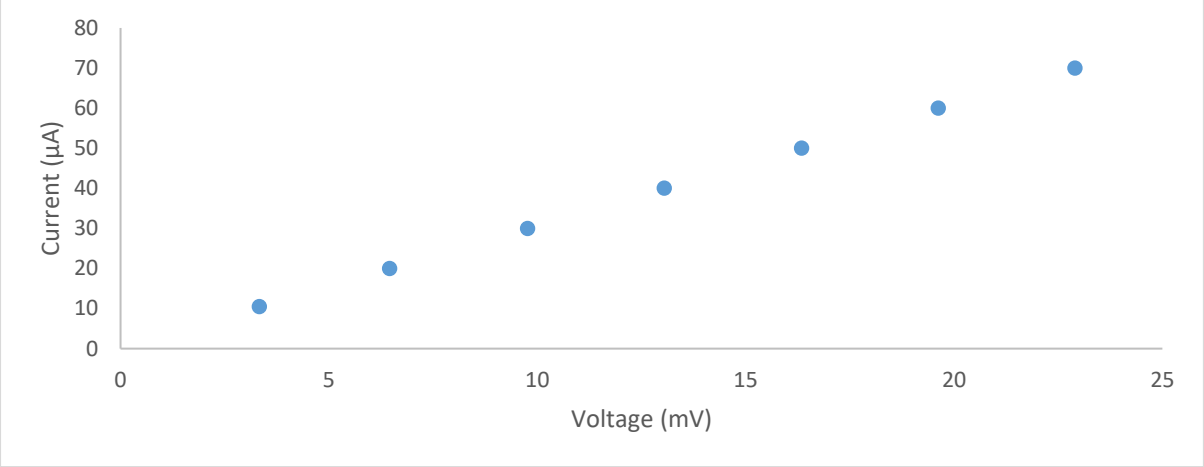

Figure 3.3.1: I-V relationship for current suppied across the central 2 μm wide Hall channel and voltage measured across two contacts seperated by 8 μm. Resistance = 679.3 Ω.

4-contact measurements were performed on two Hall bar devices by connecting a current across the furtherest apart conducting contacts on each Hall bar plotting Voltage across a series of working contacts on each device and determining sheet resistivity, R_S through the following equation:

$$Rs = \frac{\Delta R}{\Delta L} W \qquad \text{Equation 3.3.1}$$

[25] Graphene hall bar devices were destroyed by the spike in current when turning the source on. This was noted for further studies.

Where, W is the Hall channel thickness, ΔR is the change in longtitudinal resistance determined through I-V plots with change in intercontact distance ΔL. The sheet resistivity was determined for two graphene Hall channels from the same sample of commercially available graphene characterised in Section 3.1.2 by plotting ΔR vs ΔL plotted in Figure 3.3.2.

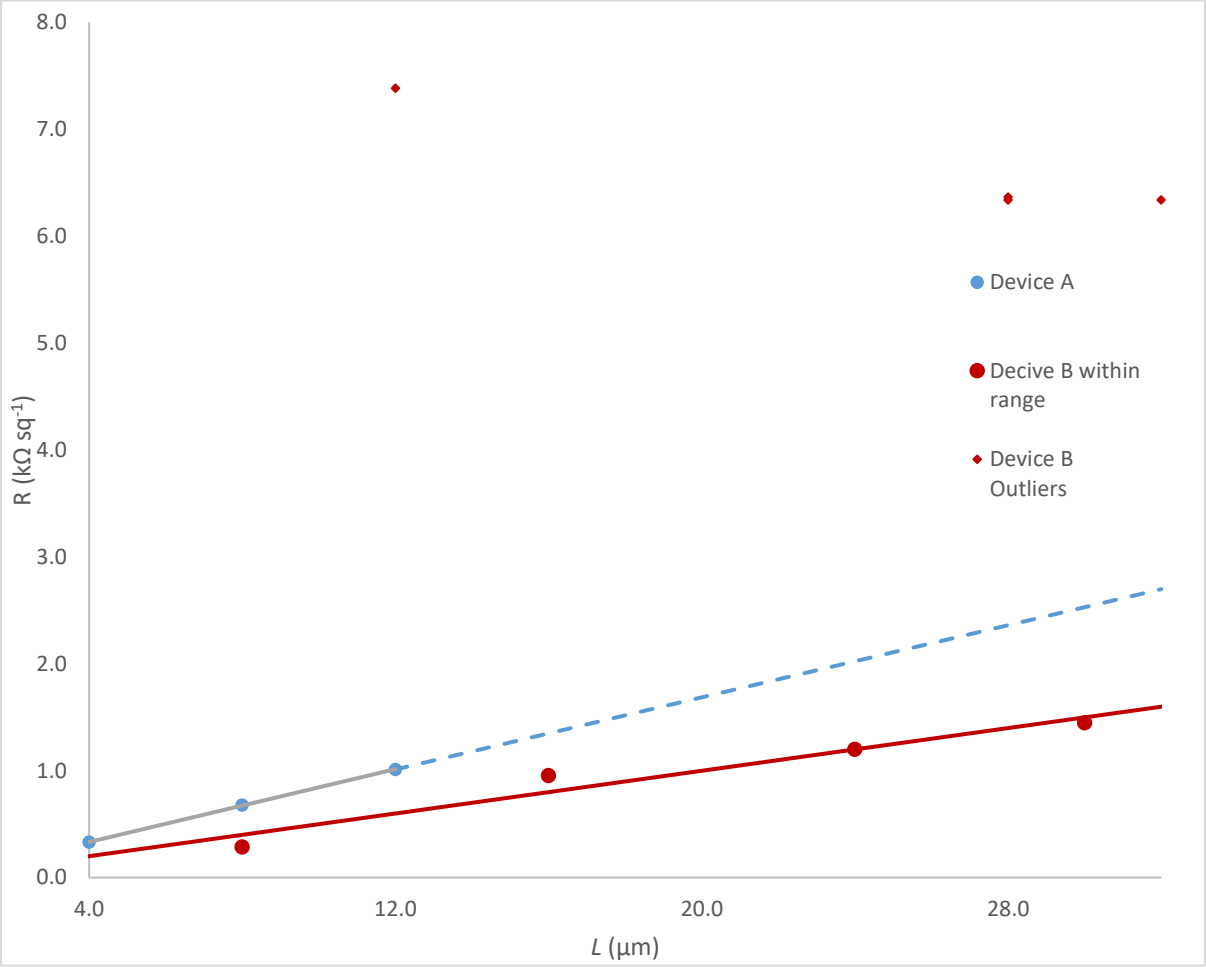

Figure 3.3.2: Relationship between inter-contact distance and resistance determined using I-V relationships for two graphene devices A and B with Hall channel thicknesses of 2µm and 8µm respectively. One outlying data point for device A was not included in this plot due to it magnitude compared to other values ($L = 2\ \mu m$, $R = 16.83\ \mathrm{k\Omega}/sq$).

Figure 3.3.2 shows that sheet resistivity between specific contact pairs on each sample follows a linear relationship with increasing distance. Excluding outliers, the mean and standard deviation of sheet resistivity values for devices A and B are calculated from Equation 3.3.1: $Rs_A = 167.7 \pm 0.7\ \Omega/sq$, $Rs_B = 386.7 \pm 79.2\ \Omega/sq$. This is lower than the quoted sheet resistivity of commercially available graphene over Si/SiO_2 substrates over a 1 cm^2 area, 460 ± 40 Ω/sq. The especially low variation in sheet resistivity measured on sample A suggests that $Rs_A = 167.7 \pm 0.7\ \Omega/\mathrm{sq}$ corresponds to the sheet resistivity of wrinkle-free regions of commercial CVD graphene on Si/SiO_2. It is expected that wrinkles between other contact pairs

in the Hall channel correspond to outlier data points in Figure 3.3.2, where the sheet resistance between contact pairs increases by up to 100-fold due to discontinuities in the graphene film. This highlights the need to minimise wrinkle formation when transferring graphene onto a substrate for optimal in-plane electronic transport properties.

4 Conclusions

This MPhil thesis focussed on synthesis, transfer and lithographic processing of CVD graphene to provide insights into how the properties of CVD graphene may be optimised through characterisation, and also aimed to act as preliminary preparation for further work which involves the fabrication of graphene tunnelling heterostructures. The procedures to reliably fabricate specific architectures of graphene on Si/SiO_2 *via* wet transfer of graphene onto Si/SiO_2 and optical lithography for electrical measurements in commercial chip packages are now in place after a significant degree of method optimisation. Characterisation studies were performed to determine the properties of commercially available CVD graphene and graphene synthesised by an optimised CVD method at the University of Bath in order to determine whether the quality of each graphene source is adequate for heterostructure fabrication. The aim was to transfer graphene onto Si/SiO_2 substrates and *via* characterisation studies measure the following outputs:

- Improved electrical properties than quoted by commercial graphene datasheets (460 ± 40 Ω/*sq*)
- > 90% monolayer coverage
- Si-Graphene AFM step height < 10 nm and surface roughness << 10nm

Raman mapping was performed on commercial and non-commercial graphene, showing significantly preferential properties of commercial graphene: lower defect densities, higher monolayer graphene domain coverage and higher homogeneity of these properties. However upon wet transfer of commercial CVD graphene onto Si/SiO_2 substrates, wrinkle formation caused a severe degradation in these properties: a ~2-4 fold increase in average defect density and a ~2 fold increase in graphene thickness and a surface roughness of ~ 3.15 nm. Additionally, electrical characterisation studies suggest that whilst the sheet resistivity of non-wrinkled regions of graphene is as low as 167 Ω/sq. with a variation < 2% between different points, the localised increase in resistivity caused by wrinkles is as high as ~100 fold. This drastic increase in resistance may be explained through local discontinuities in the graphene plane due to structural defects caused by wrinkles.

The significant impact of wrinkles upon the properties and homogeneity of CVD graphene shown by electrical, AFM and Raman measurements in Sections 3.2.2 and 3.3 lead the author to consider implementing the characterisation and potentially use of non-commercial graphene

synthesised by the method described in Section 3.1.1. Whilst average defect density of non-commercial graphene on Cu is greater than the average defect density of commercial graphene post transfer, the option to anneal the Cu substrate prior to CVD, and therefore reduce or even entirely avoid wrinkle formation in wet transfer will significantly improve the local homogeneity of graphene, reducing average thickness and surface roughness. Further work may include characterisation of non-commercial graphene post-transfer, after which an informed decision about how to source graphene for use in heterostructure fabrication could be made. Once the graphene source has been chosen, heterostructures will be fabricated using one of three possible methods which have been planned out in this report. The method to be implemented for the fabrication of heterostructures, should be selected, based upon results from AFM and Raman characterisation studies of WS_2 grown on Cu and graphene on Si/SiO_2 via CVD.

As well as wrinkle formation after wet transfer, PMMA residues also remain on graphene causing p-doping which degrades the electrical properties of graphene and cause an increase in the thickness and surface roughness. Post processing residue removal techniques were investigated using AFM scans. AFM scans showed that the variation in topography caused by wrinkles was more significant that any residues. However, an AFM scan of a non-wrinkled region of graphene showed that annealing under vacuum for 5 hours at 300 C could minimise the surface roughness to as low as 0.2 nm which is ideal for heterostructure fabrication.

This project has achieved the aim of being able to fabricate graphene devices with specific architectures for electrical testing; a pre-requisite for heterostructure fabrication. Comprehensive characterisation studies have been performed on commercially available graphene; providing results which, when compared with further studies will enable an informed decision about the exact procedure for heterostructure fabrication. Furthermore, the studies show that graphene synthesised *via* the methodology present at the University of Bath shows improved sheet resistivity compared to commercially available graphene, primarily due to the reduction of surface roughness of copper prior to graphene CVD through high temperature annealing, eliminating the formation of wrinkles.

5 Future Work

The results in this MPhil may be used as pre-requisite studies for the fabrication of tunnelling heterostructures, aiding in the methodology development for CVD fabrication and lithographic processing of graphene. However, the work presented in this MPhil could be expanded upon. To list a few examples of further work which could be recommended prior to heterostructure fabrication[26]; more extensive characterisation studies in order to attain a better understanding of how to optimise the quality of CVD graphene, manipulation of the electronic properties of graphene i.e *via* back gating control of Fermi level and measurement of quantum Hall effect and how properties of graphene are affected by the CVD and transfer process as studies prior to heterostructure fabrication.

Electrical characterisation of a larger sample of graphene Hall bars fabricated from CVD graphene produced by the Johnson group and commercially available graphene including Hall effect and field effect measurements would serve to provide electronic properties such as charge carrier mobility and density for comparisons post processing and furthermore set up the methodology for Fermi level control via back-gating and magnetic modulation. Since Raman and electrical measurements have shown that the properties of graphene show a significant dependence upon the formation of graphene wrinkles during wet-transfer, results from the characterisation of commercial and non-commercial graphene on Cu in section 3.1.2 does not necessarily relate to a comparison between the properties of commercial and non-commercial CVD graphene post transfer. Therefore, a comparison of electrical properties of graphene synthesised using the methodology described in section 3.1.1 and then transferred using methodology in section 3.1.2 would be very useful to fully determine whether graphene should be purchased commercially or grown for heterostructure fabrication. In order to minimise doping and defect formation from contaminants, the CVD vessel and apparatus should be used solely for graphene synthesis.

A post-processing PMMA removal step should be added to the transfer procedure when fabricating graphene tunnelling devices to remove surface dopants and enable greater control over the tunnelling barrier height, either through high temperature annealing or dissolution in

[26] Some of these examples may not be particularly novel, but should be carried out earlier in a PhD project to minimise the risk of running into difficulties during more complex studies i.e. measuring the strain dependency of the NDR region in ambipolar transport across tunnelling heterostructures.

chloroform. Based on the outputs from the post transfer and treatment characterisation of commercial and non-commercial graphene i.e. surface roughness, sheet resistivity, charge carrier motilities, defect density, monolayer coverage, and the homogeneity of each of these properties, the source of graphene for heterostructure fabrication can be selected. AFM results have also shown that often residues/contaminants > 10nm in height remain on graphene post treatment which could compromise the tunnelling mechanism of heterostructures. Further AFM scans after processing entirely in a clean environment could show whether these contaminants may be avoided; if they remain, mechanical cleaning using an AFM tip remains a possibility for future work.

Prior to heterostructure fabrication, AFM and Raman measurements to determine and compare the topography and continuity of WS_2 films grown on Graphene on Si and directly on Cu substrates should be performed[27]. Film continuity may be determined by Raman mapping and AFM scans to find the average thickness and surface roughness of the WS_2 films.

Three routes for heterostructure fabrication have been developed based on the knowledge and experience gained throughout this MPhil. Depending on the results of further characterisation one of three possible heterostructure fabrication methods could be employed. If the continuity and topographic properties of WS_2 grown on graphene on Si/SiO_2 substrates is acceptable (100 % continuous, average thickness <10 nm and surface roughness << 10 nm respectively), the method shown in Figure 5.1 should be used, since it is the simplest option. The possibility of mechanical cleaning after a PMMA removal step is included in each possible method and would be included in the procedure depending on the further AFM characterisation studies.

[27] The growth of WS_2 on graphene has been achieved by Mr. Joe Thompson from the Johnson group; further growth parameter optimisation may be necessary prior to AFM and Raman characterisation.

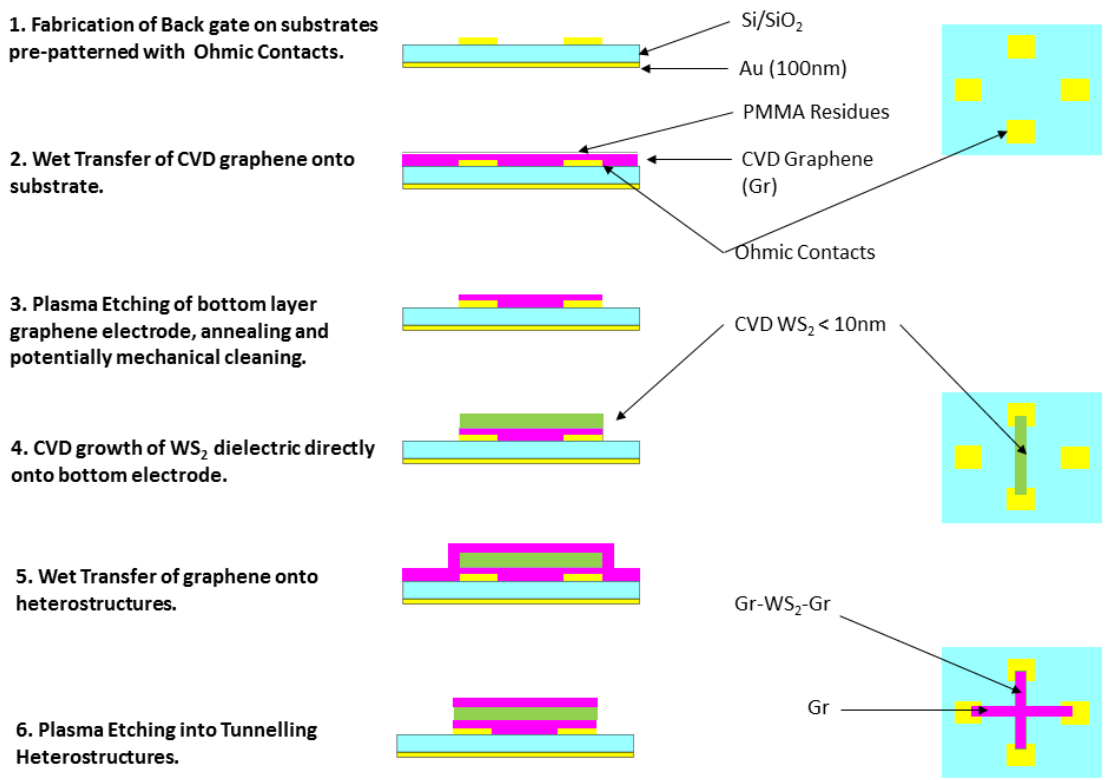

Figure 5.1: Steps towards fabrication of graphene –WS_2 –graphene heterostructures using direct CVD growth of WS_2 onto graphene.

In the case that continuous low roughness WS_2 cannot be grown on graphene on Si/SiO_2 reliably below the specified thickness two other possible options remain. In the case that WS_2 growth can be controlled within the desired parameters on Cu substrates, the method shown in Figure 5.2 should be employed.

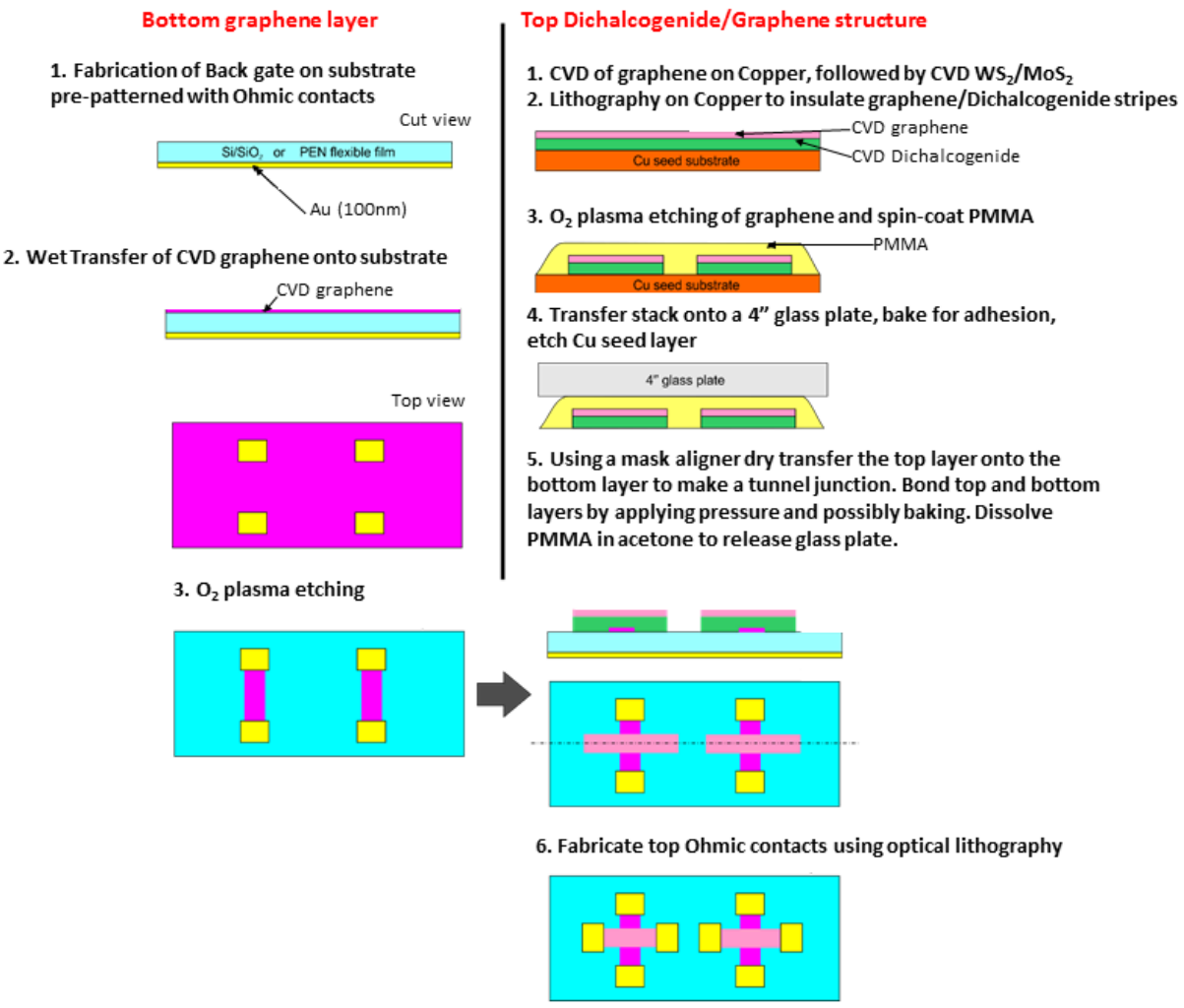

Figure 5.2: Steps towards fabrication of graphene –WS_2 – graphene heterostructures using CVD growth of WS_2 onto graphene on Cu substrates followed etching and by dry transfer onto bottom graphene electrodes.

If the growth of WS_2 on graphene on Si/SiO_2 and Cu is unsuccessful, a similar method to that shown in Figure 5.2 may be used, instead employing a polymer dielectric which is spun coat onto graphene post-etch. The procedure is shown in Figure 5.3.

Another likely further route of investigation for a project involving graphene based heterostructure electronics is to use a constant perpendicular magnetic field to modulate the thermodynamic and electronic transport properties of graphene. The application of perpendicular magnetic fields leads to oscillations in the electronic density of states through Landau quantization of graphene. This is because perpendicular magnetic modulation lifts the degeneracy of the Landau levels in graphene into bands with a bandwidth which oscillates with magnetic field strength. This work would apply perpendicular magnetic fields by using optical

lithography and thermal evaporation to deposit a strip of permalloy on each side of CVD graphene[28]. This will allow unprecedentedly high magnetic modulation since magnetic modulation may occur on both sides graphene and the magnetic strips are very close to each other, separated by only 1 sheet of graphene (~0.385nm) [61]. The large, tuneable magnetoresistance of graphene which arises through magnetic modulation shows potential for logic-based electronics[60].

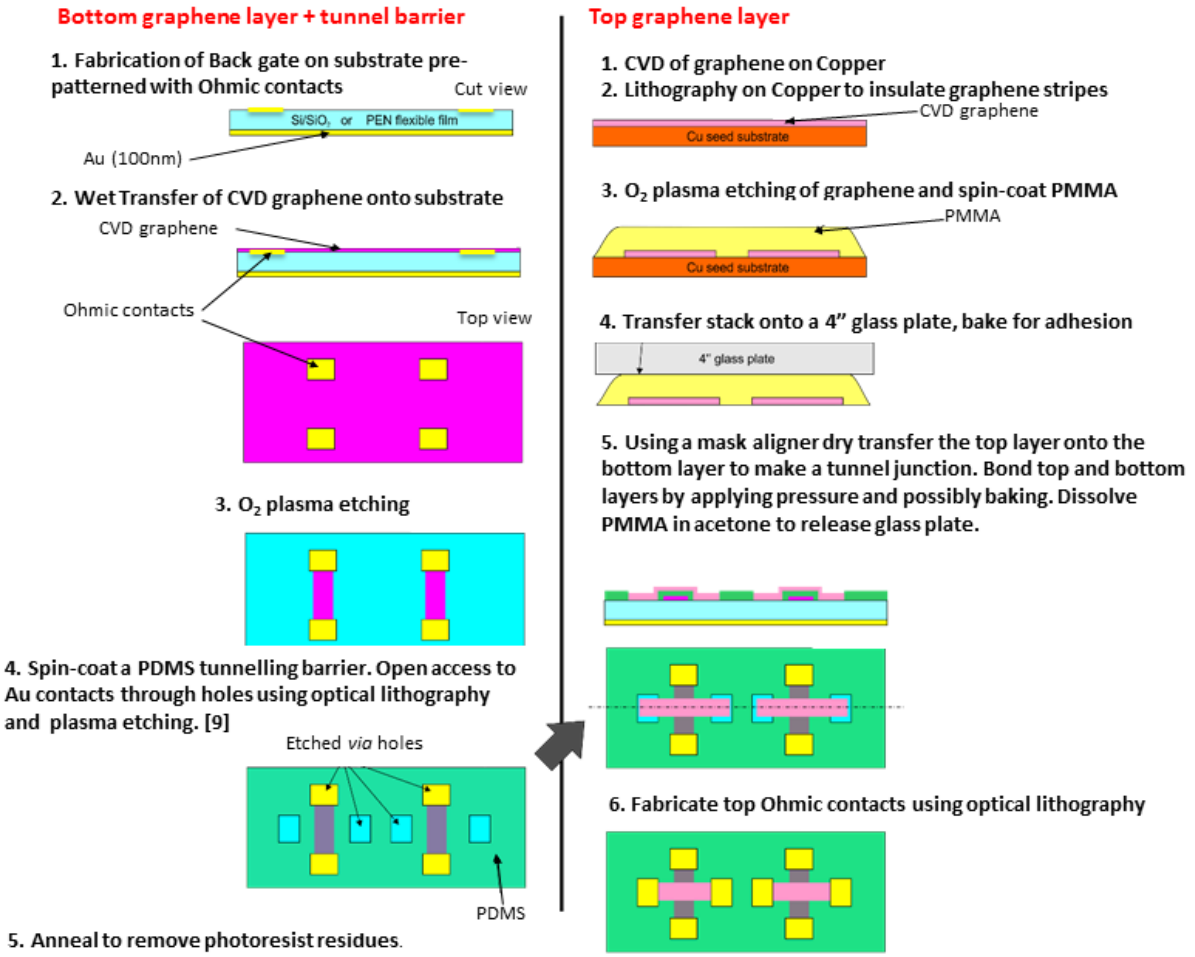

Figure 5.3: Proposed procedure for fabricating Gr-Di-Gr Heterostructures using Polydimethylsiloxane (PDMS) as a dielectric. Etching of PDMS is achieved using a O_2:CF_4 (1:3) plasma mixture [11]

[28] The optical mask currently being used for Hall bar fabrication has a design for magnetic strips.

References

1. Brattain, W.H. and B. John, *Three-electrode circuit element utilizing semiconductive materials*. 1950, Google Patents.

2. Forbes. *The world's most valuable brands*. 2015; Available from: http://www.cownetworth.com/samsung-net-worth/.

3. Moore, G.E., C*ramming more components onto integrated circuits*, Reprinted from Electronics, volume 38, number 8, April 19, 1965, pp.114 ff. Solid-State Circuits Society Newsletter, IEEE, 2006. **11**(5): p. 33-35.

4. Shao, Y., et al., *Graphene Based Electrochemical Sensors and Biosensors: A Review*. Electroanalysis, 2010. **22**(10): p. 1027-1036.

5. Yu, A., et al., *Ultrathin, transparent, and flexible graphene films for supercapacitor* application. Applied Physics Letters, 2010. **96**(25): p. 253105.

6. Nogaret, A., *Negative differential conductance materials for flexible electronics.* Journal of Applied Polymer Science, 2014. **131**(24).

7. Soldano, C., A. Mahmood, and E. Dujardin, *Production, properties and potential of graphene.* Carbon, 2010. **48**(8): p. 2127-2150.

8. Zhang, B., et al., *Large-scale production of high-quality graphene using glucose and ferric chloride*. Chemical Science, 2014. **5**(12): p. 4656-4660.

9. Britnell, L., et al., *Resonant tunnelling and negative differential conductance in graphene transistors*. Nat Commun, 2013. **4**: p. 1794.

10. Lee, J.-H., et al., *Wafer-Scale Growth of Single-Crystal Monolayer Graphene on Reusable Hydrogen-Terminated Germanium*. Science, 2014. **344**(6181): p. 286-289.

11. Garra, J., et al., *Dry etching of polydimethylsiloxane for microfluidic systems.* Journal of Vacuum Science & Technology A, 2002. **20**(3): p. 975-982.

12. Sun, Z., et al., *Growth of graphene from solid carbon sources.* Nature, 2010. **468**(7323): p. 549-552.

13. Ferrari, A.C., Raman spectroscopy of graphene and graphite: *Disorder, electron–phonon coupling, doping and nonadiabatic effects.* Solid State Communications, 2007. **143**(1–2): p. 47-57.

14. Dresselhaus, M.S., et al., *Defect characterization in graphene and carbon nanotubes using Raman spectroscopy.* Philosophical Transactions: Mathematical, Physical and Engineering Sciences, 2010. **368**(1932): p. 5355-5377.

15. Littlejohn, S., *Electromechanical Sensing*, in *Physics*. 2012, University of Bath: University of Bath.

16. Jens Christian, J., et al., *Electron–phonon coupling in quasi-free-standing graphene.* Journal of Physics: Condensed Matter, 2013. **25**(9): p. 094001.

17. Reich, S., et al., *Tight-binding description of graphene.* Physical Review B, 2002. **66**(3): p. 035412.

18. Castro Neto, A.H., et al., *The electronic properties of graphene.* Reviews of Modern Physics, 2009. **81**(1): p. 109-162.

19. Novoselov, K.S., et al., *Two-dimensional gas of massless Dirac Fermions in graphene.* Nature, 2005. **438**(7065): p. 197-200.

20. McCann, E., D.S.L. Abergel, and V.I. Fal'ko, *Electrons in bilayer graphene.* Solid State Communications, 2007. **143**(1–2): p. 110-115.

21. Zhang, Y., et al., *Direct observation of a widely tunable bandgap in bilayer graphene.* Nature, 2009. **459**(7248): p. 820-823.

22. Chung, D.D.L., *Review Graphite.* Journal of Materials Science, 2002. **37**(8): p. 1475-1489.

23. Tetlow, H., et al., *Growth of epitaxial graphene: Theory and experiment.* Physics Reports, 2014. **542**(3): p. 195-295.

24. Enderlein, C., *Graphene and its Interaction with Different Substrates Studied by Angular-Resolved Photoemission Spectroscopy* : . 2010, Freie Universität: Berlin.

25. Unarunotai, S., et al., *Transfer of graphene layers grown on SiC wafers to other substrates and their integration into field effect transistors.* Applied Physics Letters, 2009. **95**(20): p. 202101.

26. Yu, Q., et al., *Graphene segregated on Ni surfaces and transferred to insulators.* Applied Physics Letters, 2008. **93**(11): p. 113103.

27. Reina, A., et al., Large Area, Few-Layer Graphene Films on Arbitrary Substrates by Chemical Vapor Deposition. Nano Letters, 2009. **9**(1): p. 30-35.

28. De Arco, L.G., et al., *Synthesis, Transfer, and Devices of Single- and Few-Layer Graphene by Chemical Vapor Deposition*. Nanotechnology, IEEE Transactions on, 2009. **8**(2): p. 135-138.

29. Kim, E., et al., *Growth of Few-Layer Graphene on a Thin Cobalt Film on a Si/SiO2 Substrate.* Chemical Vapor Deposition, 2011. **17**(1-3): p. 9-14.

30. Yong, V. and H.T. Hahn, *Graphene growth with giant domains using chemical vapor deposition.* CrystEngComm, 2011. **13**(23): p. 6933-6936.

31. Yuan, Q., et al., *Magic Carbon Clusters in the Chemical Vapor Deposition Growth of Graphene.* Journal of the American Chemical Society, 2012. **134**(6): p. 2970-2975.

32. Massalski, T.B.O., H.; Subramanian, P. R.; and L. Kacprzak, Eds, *ASM Handbook: Alloy Phase Diagrams*. ASM International. Vol. 3. 2002, Materials Park, OH.

33. Soo Min, K., et al., *The effect of copper pre-cleaning on graphene synthesis.* Nanotechnology, 2013. **24**(36): p. 365602.

34. Ibrahim, A., et al., *Effects of annealing on copper substrate surface morphology and graphene growth by chemical vapor deposition.* Carbon, 2015. **94**: p. 369-377.

35. Jin, Y., et al., *Roles of H2 in annealing and growth times of graphene CVD synthesis over copper foil.* Journal of Materials Chemistry A, 2014. **2**(38): p. 16208-16216.

36. Wu, Z.T., et al., *The influence of chemical solvents on the properties of CVD graphene.* Journal of Raman Spectroscopy, 2015. **46**(1): p. 21-24.

37. Woosuk Choi, Y.-S.S., Jun-Young Park, K. B. Kim, Jongwan Jung, Naesung Lee, Yongho Seo, and a.S. Hong, *Effect of Annealing in Ar/H2 Environment on Chemical Vapor Deposition-Grown Graphene Transferred With Poly (Methyl Methacrylate).* IEEE TRANSACTIONS ON NANOTECHNOLOGY,, 2015. **14**(1).

38. Cheng, Z., et al., *Toward intrinsic graphene surfaces: a systematic study on thermal annealing and wet-chemical treatment of SiO2-supported graphene devices*. Nano Lett, 2011. **11**(2): p. 767-71.

39. Blake, P., et al., *Making graphene visible.* Applied Physics Letters, 2007. **91**(6): p. 063124.

40. Jia, C., et al., *Direct Optical Characterization of Graphene Growth and Domains on Growth Substrates*. Scientific Reports, 2012. **2**: p. 707.

41. Bachmatiuk, J.H.W.F.S.M.R.A., *Graphene fundamentals and emergent applications.* 2015.

42. Wirtz, L. and A. Rubio, *The phonon dispersion of graphite revisited.* Solid State Communications, 2004. **131**(3–4): p. 141-152.

43. Maultzsch, J., et al., *Phonon Dispersion in Graphite.* Physical Review Letters, 2004. **92**(7): p. 075501.

44. Saito, R.R., G. Dresselhaus, and M.S. Dresselhaus, *Physical Properties of Carbon Nanotubes*. 1998.

45. Malard, L.M., et al., *Raman spectroscopy in graphene.* Physics Reports, 2009. **473**(5–6): p. 51-87.

46. Pauw, L.J.v.d., *A Method of Measuring Specific Resistivity and Hall Effect of Discs of Arbitrary Shape*. Philips Research Reports, 1958. **13**: p. 1-9.

47. Luo, Z., et al., *Effect of Substrate Roughness and Feedstock Concentration on Growth of Wafer-Scale Graphene at Atmospheric Pressure.* Chemistry of Materials, 2011. **23**(6): p. 1441-1447.

48. Lucchese, M.M., et al., *Quantifying ion-induced defects and Raman relaxation length in graphene.* Carbon, 2010. **48**(5): p. 1592-1597.

49. R. M. Halverson, M.W.M., W. T. Motsiff *The mechanism of single-step liftoff with chlorobenzene in a diazo-type resist.* IBM J. Res. Dev., 1982. **26**(5): p. 590-595.

50. Nelson, J.K., *Dielectric polymer nanocomposites*. 2010, New York; London: Springer.

51. Broadbent, S.R. and J.M. Hammersley, *Percolation processes.* Mathematical Proceedings of the Cambridge Philosophical Society, 1957. **53**(03): p. 629-641.

52. Cappuccio, R., et al., *A parallel implementation of a cellular automata based model for coffee percolation.* Parallel Computing, 2001. **27**(5): p. 685-717.

53. Solomon, S., et al., *Social percolation models.* Physica A: Statistical Mechanics and its Applications, 2000. **277**(1–2): p. 239-247.

54. Kirkpatrick, S., *Percolation and Conduction.* Reviews of Modern Physics, 1973. **45**(4): p. 574-588.

55. L. S. Schadler, X.W., J. Nelson, and H. Hillborg, *Background, principles and promise of nanodielectrics, in Dielectric Polymer Nanocomposites*. 2010, Springer: New York.

56. Toker, D., et al., *Tunneling and percolation in metal-insulator composite materials.* Physical Review B, 2003. **68**(4): p. 041403.

57. Littlejohn, S., *Electrical Properties of Graphite* N*anoparticles in Silicone:Flexible Oscillators and Electromechanical Sensing Thesis* (Doctor of Philosophy (PhD)), in Physics. 2013, University of Bath.

58. Littlejohn, S., *Tunneling Negative Differential Resistance in a GSC, in Electrical Properties of Graphite Nanoparticles in Silicone.* 2013, Springer. p. 63-83.

59. Maricich, S.M., et al., *Merkel Cells Are Essential for Light-Touch Responses.* Science, 2009. **324**(5934): p. 1580-1582.

60. Islam, S.K.F., K.S. Naveen, and G. Tarun Kanti, *Thermodynamic properties of a magnetically modulated graphene monolayer.* Journal of Physics: Condensed Matter, 2011. **23**(44): p. 445502.

61. Nemes-Incze, P., et al., *Anomalies in thickness measurements of graphene and few layer graphite crystals by tapping mode atomic force microscopy.* Carbon, 2008. **46**(11): p. 1435-1442.

62. Miseikis, V., et al. (2015). *"Rapid CVD growth of millimetre-sized single crystal graphene using a cold-wall reactor."* 2D Materials 2(1): 014006.

63. Ogawa, Y., et al. (2012). *"Domain Structure and Boundary in Single-Layer Graphene Grown on Cu(111) and Cu(100) Films."* The Journal of Physical Chemistry Letters 3(2): 219-226.

64. Nguyen, V. L., et al. (2015). *"Seamless stitching of graphene domains on polished copper (111) foil."* Adv Mater 27(8): 1376-1382.

65. Goossens, A. M., et al. (2012). *"Mechanical cleaning of graphene."* Applied Physics Letters 100(7): 073110.

66. Zhu, W., et al. (2012). *"Structure and Electronic Transport in Graphene Wrinkles."* Nano Letters 12(7): 3431-3436.

67. Robertson, A. W. and J. H. Warner (2011). *"Hexagonal Single Crystal Domains of Few-Layer Graphene on Copper Foils."* Nano Letters 11(3): 1182-1189.

68. Wang, H., et al. (2010). *"Hysteresis of Electronic Transport in Graphene Transistors."* ACS Nano 4(12): 7221-7228.

69. Graphenea (2014). *"Product Datasheet Graphene a Monolayer Graphene film on various substrates*." Retrieved 10/03/2016, 2016, from http://www.graphenea.com/.

70. K.I. Bolotina, K. S. (2008*). Ultrahigh electron mobility in suspended graphene*. Solid State Comminications, Volume 146, pp 351-355.

71. Van der Pauw. (958). *A method of measuring the resisitivuty and hall coeficcient of lamellae of arbitrary shape*. Philippes Technical Review Volume 26, pp 220-225.

72. E. McCann and M. Koshimo (2013). *"The Electronic Properties of Bilayer Graphene*." Reports of Progress in Physics, Volume 76(5)

73. A. H. Castro Neto., et al (2009). *"The Electronic Properties of Graphene*." Reviews of Modern Physics, Volume 81

Annex A. **Tight Binding Model of Graphene:**

To plot an energy band diagram of the BZ of graphene in order to understand electronic properties, Schrodinger's equation must be solved;

$$\hat{\mathrm{H}}\Psi(\vec{k}) = \mathrm{E}(\vec{k})\Psi(\vec{k})$$

where $\hat{\mathrm{H}}$ is the Hamiltonian; $-\frac{\hbar^2}{2m}\nabla^2 + v$

$\mathrm{E}(k)$ and $\Psi(\vec{k})$ are the energy eigenvalues and eigenfunctions of wavevector $\vec{k}$ respectively.

The eigenfunctions can be given in the Tight Binding model through the superposition of two Bloch functions, which each approximate the wavefunction of electrons in two respective sub-lattices.

$$\Psi(\vec{k}) = \sum_i C_i \Phi_i(\vec{k}) \qquad \text{Equation 1}$$

The Bloch functions are given by a linear summation of atomic orbitals at each site within the respective sub-lattices. In the case of graphene there are two sub-lattices, denoted A and B. Bloch functions for sub-lattice A and B are constructed:

$$\Phi_A = \frac{1}{\sqrt{N}} \sum_{R_A} e^{ik.R_A} \varphi(r - R_A) \qquad \text{Equation 2}$$

$$\Phi_B = \frac{1}{\sqrt{N}} \sum_{R_B} e^{ik.R_B} \varphi(r - R_B) \qquad \text{Equation 3}$$

where r is a position vector, $R_{A/B}$ is a lattice vector in sub-lattice A/B and N is the total number of atoms in the crystal.

The Bloch functions are summed and then substituted into Schrodinger's Equation (Equation 4) to find the energy eigenvalues *E(k)*.

$$H\Psi(\vec{k}) = E(\vec{k})\Psi(\vec{k}) \qquad \text{Equation 4}$$

$$H(C_A.\Phi_A + C_B.\Phi_B) - E(k)(C_A.\Phi_A + C_B.\Phi_B) = 0 \qquad \text{Equation 5}$$

where H is the Hamiltonian; $-\frac{\hbar^2}{2m}\nabla^2 + v$

Multiplying Equation 5 by ${\Phi_A}^*$ and ${\Phi_B}^*$ and integrating over the entire crystal provides the following simultaneous equations:

$$C_A[H_{AA} - ES_{AA}] + C_B[H_{AB} - ES_{AB}] = 0 \quad \text{Equation 6}$$

$$C_A[H_{BA} - ES_{BA}] + C_B[H_{BB} - ES_{BA}] = 0 \quad \text{Equation 7}$$

where,

$$H_{mn} = \int_0^\infty {\Phi_m}^* H \Phi_n = \langle \Phi_m | H | \Phi_n \rangle \quad \text{Equation 8}$$

$$S_{mn} = E\int_0^\infty {\Phi_m}^* \Phi_n = E\langle \Phi_m | \Phi_n \rangle. \quad \text{Equation 9}$$

The simultaneous equations are simplified in order to make it easier to find a solution. H_{AA} and H_{BB} are identical since the distribution of atoms in the A and B sub-lattices throughout a crystal are the same. Similarly, $S_{AA} = S_{BB}$ and $H_{AB} = {H_{BA}}^*$. The simplified matrix equation is given below:

$$\begin{bmatrix} H_{AA} - ES_{AA} & H_{AB} - ES_{AB} \\ {H_{AB}}^* - E{S_{AB}}^* & H_{AA} - ES_{AA} \end{bmatrix} \cdot \begin{bmatrix} C_A \\ C_B \end{bmatrix} = 0 \quad \text{Equation 10}$$

The matrix equation is solved for the non-trivial *E(k)* solutions.

$$E^2\left({S_{AA}}^2 - S_{AB}{S_{AB}}^*\right) + E(H_{AB}{S_{AB}}^* + S_{AB}{H_{AB}}^* - 2EH_{AA}S_{AA}) + {H_{AA}}^2 - H_{AB}{H_{AB}}^* = 0 \quad \text{Equation 11}$$

Using the quadratic formula expressions for the energy dispersion bands are determined where $E(k)^-$ the energy eigenvalue of the valence band is and $E(k)^+$ is the energy eigenvalue of the conduction band.

$$E(k)^{\pm} = {-(E_1 - 2E_0) \pm \sqrt{(E_1 - 2E_0)^2 - 4E_2E_3}}\Big/{2E_3} \quad \text{Equation 12}$$

Where,

$$E_0 = H_{AA}S_{AA} \quad \text{Equation 13}$$

$$E_1 = S_{AB}{H_{AB}}^* + H_{AB}{S_{AB}}^* \quad \text{Equation 14}$$

$$E_2 = {H_{AA}}^2 - H_{AB}{H_{AB}}^* \quad \text{Equation 15}$$

$$E_3 = {S_{AA}}^2 - S_{AB}{S_{AB}}^* \quad \text{Equation 16}$$

Considering only nearest-neighbour interactions, H_{mn} and S_{mn} are calculated explicitly from the Bloch functions in Equation 2 and Equation 3. Starting with H_{AA}:

$$H_{AA} = \frac{1}{N}\sum_{R_A}\sum_{R_A{}'}\left\langle e^{ik.R_A}\varphi(r-R_A)\middle|H\middle|e^{ik.R_A{}'}\varphi(r-R_A{}')\right\rangle \quad \text{Equation 17}$$

The first summation is performed over all carbon atoms, *N*, in sub-lattice A. The second summation accounts for all atoms in an A sub-lattice which are first nearest neighbours with the atom being considered in the first sum.

The positions of the nearest neighbour atomic sites relative to a central atom at an A sub-lattice atomic site in a graphene crystal is shown in figure 2.2.1. All 1st order nearest neighbours of an atomic site belonging to sub-lattice A belong to the sub-lattice B, therefore the second summation in Equation 17 only includes the summation with itself i.e. $R_A{}' = R_A$. H_{AA} is therefore given as an empirical constant given below:

$$\tfrac{1}{N}\textstyle\sum_{R_A} e^{ik.(R_A-R_A)}\,\langle\varphi(r-R_A)|H|\varphi(r-R_A)\rangle = \quad \text{Equation 18}$$

$$\frac{1}{N}N\langle\varphi(r-R_A)|H|\varphi(r-R_A)\rangle = \varepsilon_{2p}$$

ε_{2p} is an empirical constant which is calculated through comparisons with the bandstructure found through the nearest neighbour tight-binding model and experimental results or Density Function Theory (DFT) calculations. Similarly assuming the atomic orbitals of the carbon atoms in graphene are normalised;

$$S_{AA} = \frac{1}{N}\sum_{R_A} e^{ik.(R_A-R_A)}\langle\varphi(r-R_A)|\varphi(r-R_A)\rangle = 1 \quad \text{Equation 19}$$

The diagonal matrix elements are calculated through substitution of nearest neighbour vectors R_{1i} as shown below.

$$H_{AB} = \frac{1}{N}\sum_{R_A}\sum_{R_B}\left\langle e^{ik.R_A}\varphi(r-R_A)\middle|H\middle|e^{ik.R_B}\varphi(r-R_B)\right\rangle \quad \text{Equation 20}$$

$$H_{AB} = \left(e^{ik.R_{11}} + e^{ik.R_{12}} + e^{ik.R_{13}}\right)\frac{1}{N}\sum_{R_A}\langle\varphi(r-R_A)|H|\varphi(r-R_B)\rangle \quad \text{Equation 21}$$

Performing the substitution $\gamma_0 = \frac{1}{N}\sum_{R_A}\langle\varphi(r-R_A)|H|\varphi(r-R_B)\rangle$, where γ_0 is an empirical constant[29], and substituting nearest neighbour vectors into Equation 21.

$$R_{11} = \frac{1}{3}(2a_1 - a_2) \quad \text{Equation 22}$$

$$R_{12} = \frac{1}{3}(-a_1 + 2a_2) \quad \text{Equation 23}$$

$$R_{13} = a_0(-a_1, -a_2) \quad \text{Equation 24}$$

given

$$H_{AB} = \gamma_0\left(e^{-\frac{1}{3}ik.(a_1+a_2)}\right)\left(e^{ik.a_1} + e^{ik.a_2} + 1\right) \quad \text{Equation 25}$$

Similarly, S_{AB} is calculated as

$$S_{AB} = s_0\left(e^{-\frac{1}{3}ik.(a_1+a_2)}\right)\left(e^{ik.a_1} + e^{ik.a_2} + 1\right) \quad \text{Equation 26}$$

where

$$s_0 = \frac{1}{N}\sum_{R_A}\langle\varphi(r-R_A)|\varphi(r-R_B)\rangle.$$

The empirical constant which are determined experimentally or through DFT calculations have values: $\varepsilon_{2p} = 0, s_0 = 0$ eV[30], $\gamma_0 = 2.7$ eV [17].

The matrix elements are then substituted into terms Equation 13, Equation 14, Equation 15 and Equation 16 and simplified.

$$E_0 = \varepsilon_{2p} \quad \text{Equation 27}$$

$$E_1 = 2s_0\gamma_0 u(k) \quad \text{Equation 28}$$

$$E_2 = {\varepsilon_{2p}}^2 - {\gamma_0}^2 u(k) \quad \text{Equation 29}$$

$$E_3 = 1 - {s_0}^2 u(k) \quad \text{Equation 30}$$

Where,

[29] 3-fold symmetry of graphene sub lattices allows such a substitution to be made

[30] s_0 is small and is neglected in DFT studies performed by 17. Reich, S., et al., *Tight-binding description of graphene.* Physical Review B, 2002. **66**(3): p. 035412.

$$u(k) = 2cos(k.a_1) + 2cos(k.a_2) + 2cos\big(k.(a_1 - a_2)\big) + 3$$

In Cartesian co-ordinates in reciprocal space $u(k)$ is obtained through substitution of lattice vectors $a_{1,2}$.

$$u(x,y) = 2cos(a_0 y) + 4cos\left(\frac{\sqrt{3}a_0}{2}x\right)cos\left(\frac{a_0}{2}y\right) + 3 \qquad \text{Equation 31}$$

However, it is often simpler to use reciprocal lattice vectors:

$$u(k_1,k_2) = 2cos(2\pi.A) + 2cos(2\pi.B) + 2cos\big(2\pi.(A-B)\big) \qquad \text{Equation 32}$$

where,

$$k_1 = A.b_1$$
$$k_2 = B.b_2$$

and A and B are scalars b_1 and b_2 are the reciprocal lattice unit vectors.

Substituting terms $E_{1..3}$ into Equation 12 reveals the energy dispersion of graphene through reciprocal space:

$$E(k)^{\pm} = \frac{\varepsilon_{2p} \pm \gamma_0\sqrt{u(k_1,k_2)}}{1 \pm s_0\sqrt{u(k_1,k_2)}} \qquad \text{Equation 33}$$